High Temperature Investigations of Crystalline Silicon Solar Cell Materials

by

George David Stephen Hudelson, III

B.S. Mechanical Engineering
Case Western Reserve University, 2007

Submitted to the Department of Mechanical Engineering
in Partial Fulfillment of the Requirements for the Degree of
Master of Science in Mechanical Engineering

at the

Massachusetts Institute of Technology

June 2009

Signature of Author.....
Department of Mechanical Engineering
May 12, 2009

Certified by.....
Tonio Buonassisi
Assistant Professor of Mechanical Engineering
Thesis Supervisor

Accepted by.....
David E. Hardt
Professor of Mechanical Engineering
Graduate Officer

Defect Engineering in Multicrystalline Silicon Solar Cells

by

George David Stephen Hudelson, III

Submitted to the Department of Mechanical Engineering
on May 12, 2009 in Partial Fulfillment of the
Requirements for the Degree of Master of Science in
Mechanical Engineering

ABSTRACT

Crystalline silicon solar cells are a promising candidate to provide a sustainable, clean energy source for the future. In order to bring about widespread adoption of solar cells, much work is needed to reduce their cost. Herein, I discuss the development of a new experimental technique to investigate solar cell materials under simulated processing conditions. I present the first applications and results using this technique, including observations of novel impurity interactions at elevated temperatures, and discuss their importance to the solar cell manufacturing process.

One of the key drivers for reducing solar cell cost is developing a fundamental understanding of the behavior of defect and impurities in solar cell materials. Since solar cell processing occurs at high temperatures, experiments are needed that allow characterization of solar cell materials at high temperatures representative of manufacturing conditions, at the length-scales of the defects that are present. To achieve this, I have developed a novel *in situ* high temperature sample stage for measuring samples via synchrotron-based X-ray microprobe. This technique allows for mapping and chemical state determination of metal impurity clusters on the order of 100 nm to 100 μm, over sample areas of several square millimeters, at temperatures in excess of 1200°C and under controlled ambient atmosphere.

The application of this technique has yielded novel insights concerning the behavior of metal impurities at high temperature. For the first time, the phenomenon of retrograde melting (i.e. melting on cooling) has been observed in a semiconductor material. Internal gettering of dissolved metal to liquid metal-silicon droplets within the silicon matrix is observed. Understanding of this phenomenon provides the potential to improve solar cell devices by reducing the more-detrimental dissolved metal content within the material by concentrating it into precipitates. Finally, I provide results and a model that explains the formation and resulting morphology of mixed-metal silicide precipitates in multicrystalline silicon.

Thesis Supervisor: Tonio Buonassisi
Title: Professor of Mechanical Engineering

ACKNOWLEDGEMENTS

"The Lord gives wisdom. From his mouth come knowledge and understanding." (Proverbs 2:6) All that I have and all that I accomplish come from God. Above all else it is my faith that sustains me and directs me, giving meaning to everything I do. My greatest hope is that all of my work will be for the glory of God.

I dedicate my work with great love and gratitude to my wife Marianne: For taking a step out of our comfort zone to come to Boston; for the constant support without which I never would have survived MIT; for the constant patience to put up with my quirks; and for the countless other ways you've helped me along. I dedicate it also to my son James, who brings such joy into my life. I also gratefully thank my parents and family, for all that they've done to help me get where I am, and especially for encouraging me to take a chance at MIT.

I also thank Tonio, for the countless ways he has helped make my stay at MIT what it was: for taking a chance on a student without a home, and no experience in PV; for teaching me almost everything I know about solar cells; and for helping me develop in so many ways, from my scientific instinct, to presentation style and effectiveness, to writing ability.

Next, I very gratefully acknowledge the co-authors of my papers (Sarah Bernardis, Mariana Bertoni, Tonio Buonassisi, Sirine Fakra, David Fenning, Matthew Marcus, Barry Lai, and Bonna Newman) for their input, feedback, and most of all patience during the seemingly endless iterations of writing and rewriting our papers.

Additionally, Matthew Marcus and Sirine Fakra are very gratefully acknowledged for their limitless patience and support with the development and adaptation of the high temperature sample stage to beamline 10.3.2. Barry Lai and Zhonghou Cai are thanked for their assistance at Beamline 2-ID-D. J. McGinn and Sam Cortes of McCrone Scientific, and Hai-Ho at Linkam Scientific are acknowledged for their outstanding equipment support in the development of the hot stage. Matthias Heuer, Edwin L. Thomas, Sabine Langkau, Matthew Pickett, Ethan Good, Annika Zuschlag, Gianluca Coletti, Harold Dekkers, and Stephan Riepe are thanked for many enlightening discussions and suggestions.

Finally, in no particular order, I thank Richard Brickman, Mariana Bertoni, Sarah Bernardis, David Fenning, Katy Hartman, Yun Seog Lee, Bonna Newman, Jim Serdy, Jim Bredt, Amine Berrada, Eerik Hantsoo, Anjuli Appapillai, Joe Sullivan, Allie Fecych, Keith Richtman, Stephan Schoenfelder, Sebastian Castro, Sebastian Oener, Ben Pope, Jasmin Hoffstetter, Scott Speakman, and all of my 35-135 officemates and other LMP colleagues for the countless times and ways they helped me, and made life at MIT enjoyable.

CONTENTS

FIGURES

CHAPTER

1

INTRODUCTION

The motivations for development of inexpensive, domestic, and sustainable sources of energy for powering society are manifold. The reasons are widely elaborated elsewhere, and outlined below; while the precise motivation for pursuing new energy sources may vary from person to person, there is near-unanimous agreement that any one of the reasons is large enough to drive research.

1.1 Motivation for Development of New Energy Sources

The price of conventional energy, and in particular fossil-fuel sourced energy, has shown great historical volatility. Figure 1.1 shows the historical price of petroleum. In addition to the volatility of oil prices, one can also see that in recent years, the inflation corrected price of oil has begun to show an upward trend. While debate continues over whether world oil production has peaked, or whether new discoveries will continue to increase the world supply, it is agreed that eventually oil production will peak and decline accompanied by increasing oil prices. The same argument applies equally to coal and natural gas as power sources, though the time scale on which the supplies of these energy sources peak varies.

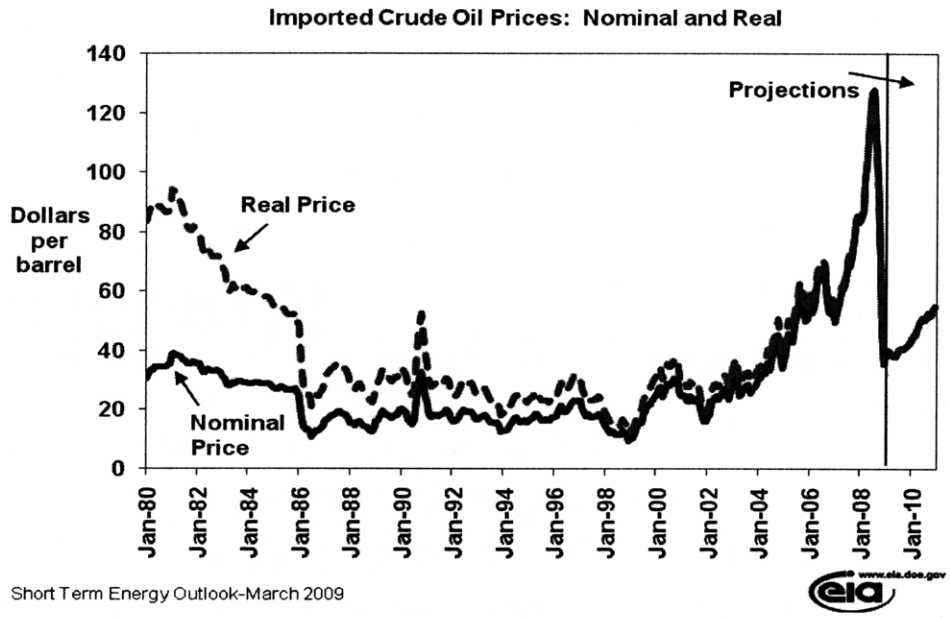

Figure 1.1: Historical petroleum prices.
The historical price of petroleum (nominal price in solid blue, real price (indexed to 1982-84 dollar) in dashed red). Figure from Reference [1].

In 2002, the United States consumes approximately 103 EJ (10^{20} J) annually [2], equivalent to approximately a quarter of the 433 EJ of worldwide primary energy consumption [3]. Over 75% of US primary energy comes from fossil fuel sources (coal, natural gas, or petroleum), as demonstrated in Figure 1.2. Coupled with the volatility of fossil fuel energy prices and eventual exhaustion of these resources, shifting away from a fossil fuel-based energy economy could provide several economic benefits.

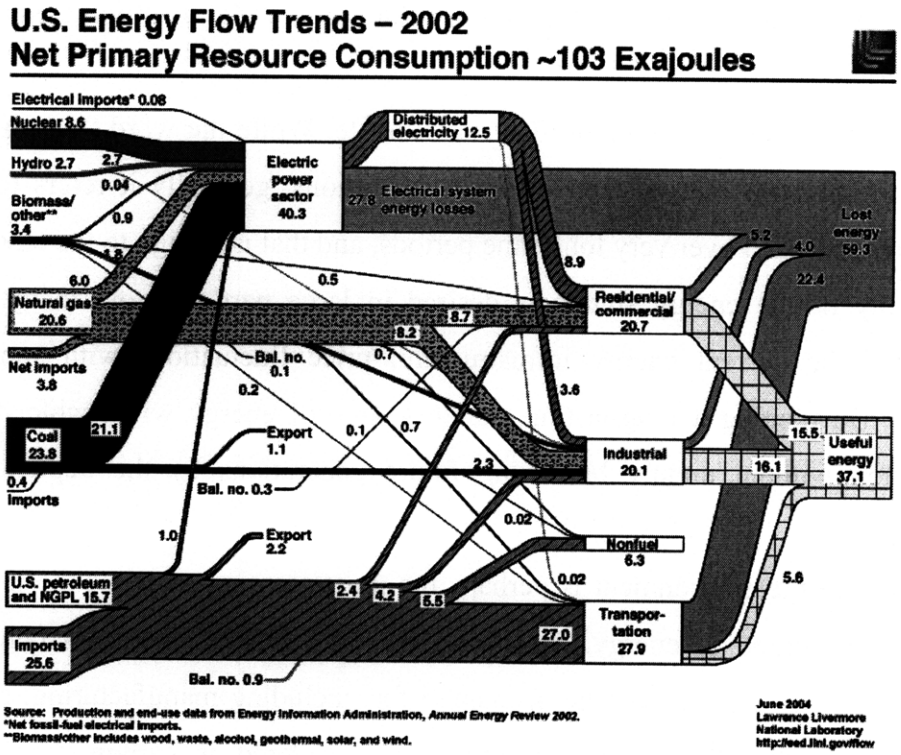

Figure 1.2: 2002 US Energy Flow.
Energy inputs broken down by energy source are show at left, and outputs broken down by end use are shown at right. Figure from Reference [2].

The price of energy is a complex issue (see, for example, [4,5]), with the source of price volatility depending on many interwoven factors. Among the most important of these factors relates to the geopolitical stability of the originating regions of an energy source. Petroleum, which originates in locations such as the Middle East, Russia, and South America, is particularly vulnerable to the effects of regional political instability. Thus, new sources of energy are desired that are more immune to such vulnerabilities. Ideally, energy sources would be domestic, allowing nations to be self-sufficient at producing their energy. In such a scenario, not only are energy prices less susceptible to volatility, but countries are also less able to use energy as a tool of conflict, as has historically often been the case.

An added benefit to domestic production of new energy sources comes from the economic stimulation that such a developing industry can create. Scientific advances and technological breakthroughs are necessary in order to bring technology to the cutting edge and make it cost competitive with current technologies. This could support the long term development of a robust research and development job market in the area of energy. As well, manufacturing jobs would be required on a large scale to implement and maintain any such

updating of the energy infrastructure of a nation, resulting in widespread job creation across the economic spectrum.

Finally, a new energy source must be sustainable. While the word "sustainable" can be used in different contexts and take on different definitions, generally it refers to a source of energy that can be utilized over very long time periods, and that is benign to the environment.

Durability of the energy source is desired in large part to avoid many of the same shortcomings of the current energy infrastructure: price fluctuations with supply, political instability, etc. Developing a long-lasting, stable source of energy will enable its use by the world population without unduly burdening future generations by the depletion of energy resources.

Benignity to the environment is perhaps the most pressing of all of the motivations for developing a new source of energy. To ensure that a source of energy is benign, the total lifecycle of the energy source must be accounted for, including manufacturing, operation, and disposal. Chief among the outputs that must be considered is carbon dioxide and other greenhouse gasses. There is widespread scientific agreement [6] that these gasses are responsible in large part for the observations of climate change on earth. Carbon-free energy sources are needed on the terawatt scale in order to meet growing global demand for energy, as well as to replace existing carbon-producing power sources.

1.2 Solar Power

1.2.1 Solar Energy Availability

Solar power is one promising technology that has the potential to meet the requirements listed above by providing a (practically) inexhaustible source of domestic, sustainable energy. Figure 1.3 shows the global exergy (the theoretical maximum extractable work available) of different renewable energy sources. These data are discussed in more detail in [7].

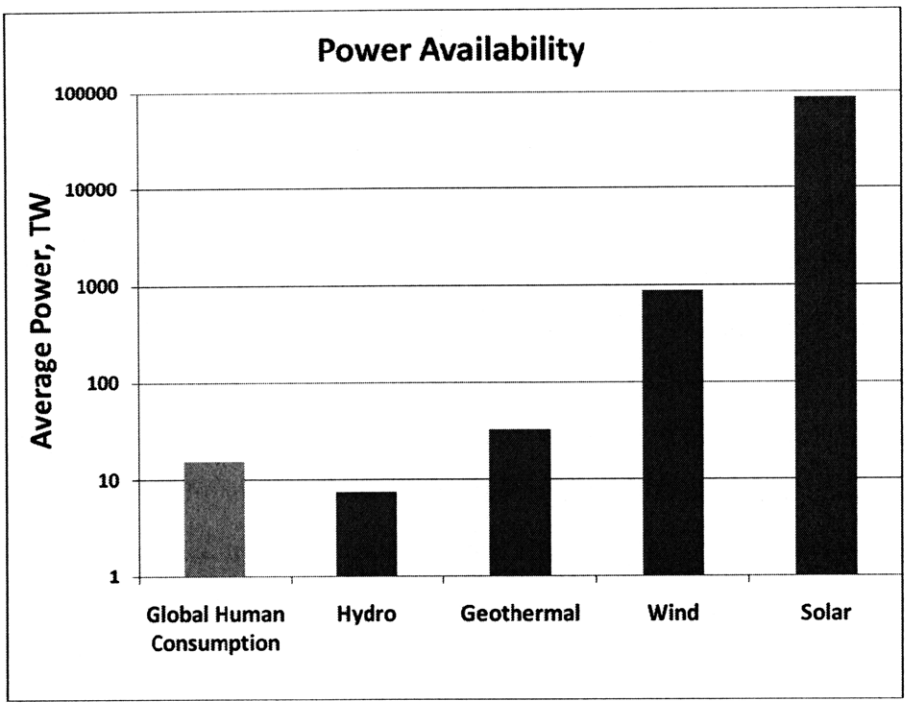

Figure 1.3: Global exergy of various renewable energy sources.
Total human power consumption is shown for comparison (Note logarithmic scale). Data are taken from Reference [7].

The amount of solar power striking the surface of earth is over 1000 times greater than the global power usage. While thermodynamics limits the efficiency of converting this energy to perform useful work, it is clear that the sun provides an abundant source of clean energy. Compared to other clean energy technologies, the abundance of solar power alone makes it an attractive option for meeting the world's growing energy needs in a sustainable way.

1.2.2 Solar Energy Conversion

In order to take advantage of the vast solar resource, the energy incident upon earth must be converted into a useful form of energy, so that it can be used to do work. There are several approaches to converting sunlight to useful work, including solar thermal, solar hydrolysis, and solar photovoltaics. Solar thermal involves converting solar photons into thermal energy. This thermal energy can then be used to directly heat buildings or water, reducing heating by other energy sources, such as direct combustion of fossil fuels. Alternatively, the thermal energy can be used to drive a heat engine, such as a Stirling engine, to produce electricity.

In solar hydrolysis [8], solar photons are used in conjunction with a catalyst in order to split water molecules, producing H_2 and O_2. H_2 can then be stored and used directly in fuel cells,

or further refined into hydrocarbons. Although this approach is promising because of its ability to convert sunlight into an energy source that is easily stored, much work and development is needed before this approach can scale to meet the global energy needs.

Finally, solar photovoltaics directly convert solar energy into electricity. In a general application of photovoltaics, a semiconductor material with a bandgap energy in the energy range of the solar spectrum. Photons incident upon the solar cell can be absorbed and create excitons (hole-electron) pairs by excitation of an electron from the valence band to the conduction band (Figure 1.4). Photons that have energy greater than the bandgap can be absorbed, but the amount of useful energy that can be collected is limited by the bandgap energy; any excess photon energy is converted to heat by thermalization as the excited electron falls to the energy minimum of the conduction band. Conversely, photons with energy below the bandgap are transmitted through the solar cell without being absorbed, and without producing work.

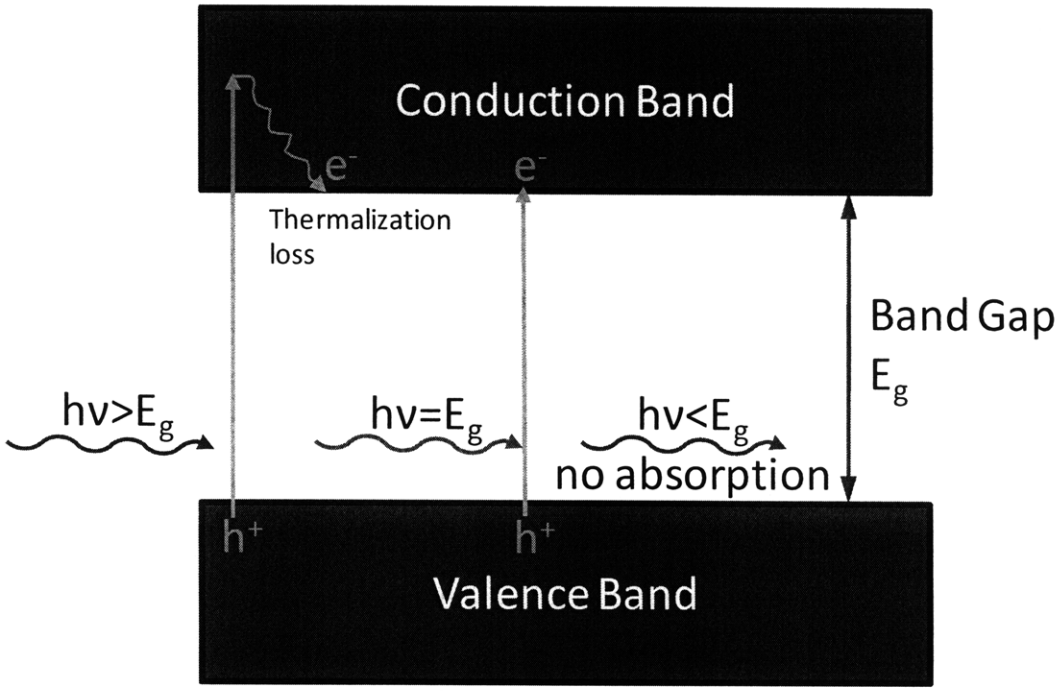

Figure 1.4: Light absorption in solar cell material.
Photons with energy greater than or equal to the bandgap can be absorbed.

The excited minority carriers are then swept to the surface of the solar cell by the pn junction, a built-in electric field in the solar cell device (Figure 1.5). Finally, they are collected

by conductive contacts at the surfaces of the solar cell, contributing to a device current that allows for work to be done by the solar cell device.

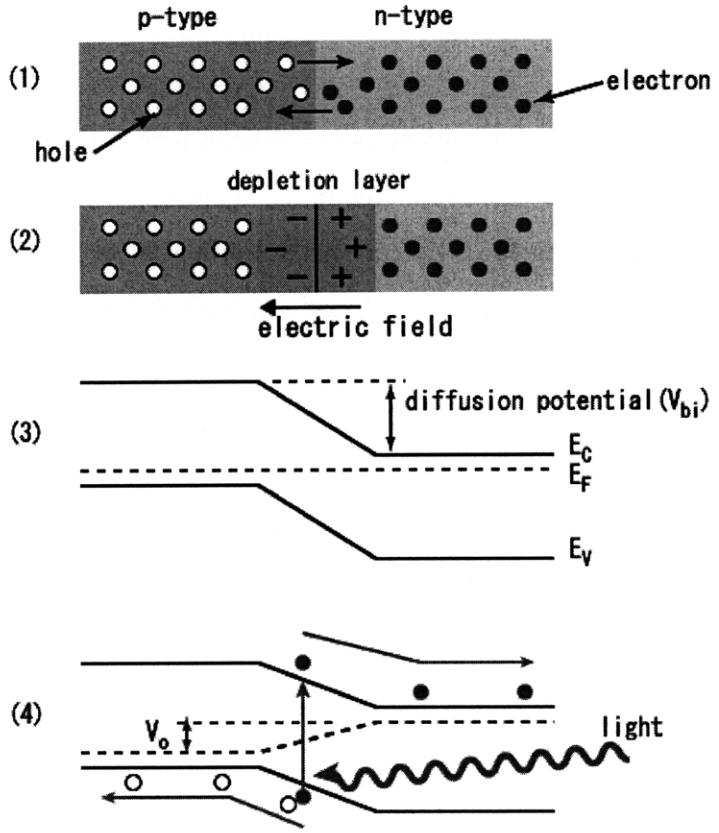

Figure 1.5: Band diagram of a solar cell.
Excited holes and electrons are separated by the electric field at the pn junction [9].

1.2.3 Photovoltaics Technologies

Photovoltaics research and manufacturing can be roughly divided into three categories, based on the technology employed: crystalline silicon, thin films, and other technologies.

1.2.3.1 Crystalline Silicon PV

The main technology used today in the production of solar cells is crystalline silicon. A good review of crystalline silicon solar cell processing is found in [10]; a brief summary of the process is detailed below.

First, silicon is mined from the earth in the form of SiO_2-bearing compounds. Via carbothermic reduction, Si is extracted and refined to "metallurgical-grade silicon" (MG-Si),

with purities of approximately 98-99% [11,12]. After this step, further refining is required to remove impurities. Traditionally, this has been performed using the energy intensive Siemens process, in which silicon in the form of trichlorosilane ($HSiCl_3$) is deposited at high temperatures onto high purity silicon rods, producing electronics-grade silicon (EG-Si) containing impurity levels lower than 10^{-7} [13].

In order to produce wafers, the polycrystalline silicon is then melted inside a crucible and directionally solidified using one of several methods, including the Czochralski method, the float-zone method, or ingot casting [13]. Directional solidification provides another purification step, since at high temperatures, the solubility of many impurities in liquid silicon is much higher than in solid silicon. This provides a driving force for the aggregation of impurities to the last mass of liquid to solidify, and the solidified silicon is purified. During this step, the silicon is also "doped" by the addition of trace amounts of dopant elements. In most crystalline silicon solar cells produced today, boron is used as the base dopant. Current efforts are underway to develop processes that allow direct production of "upgraded metallurgical grade silicon (UMG-Si) from MG-Si, bypassing the gaseous phase purification used in the production of EG-Si. If accomplished, this could lead to significant cost-savings, as well as reduction of the input energy required for production of silicon for solar cells.

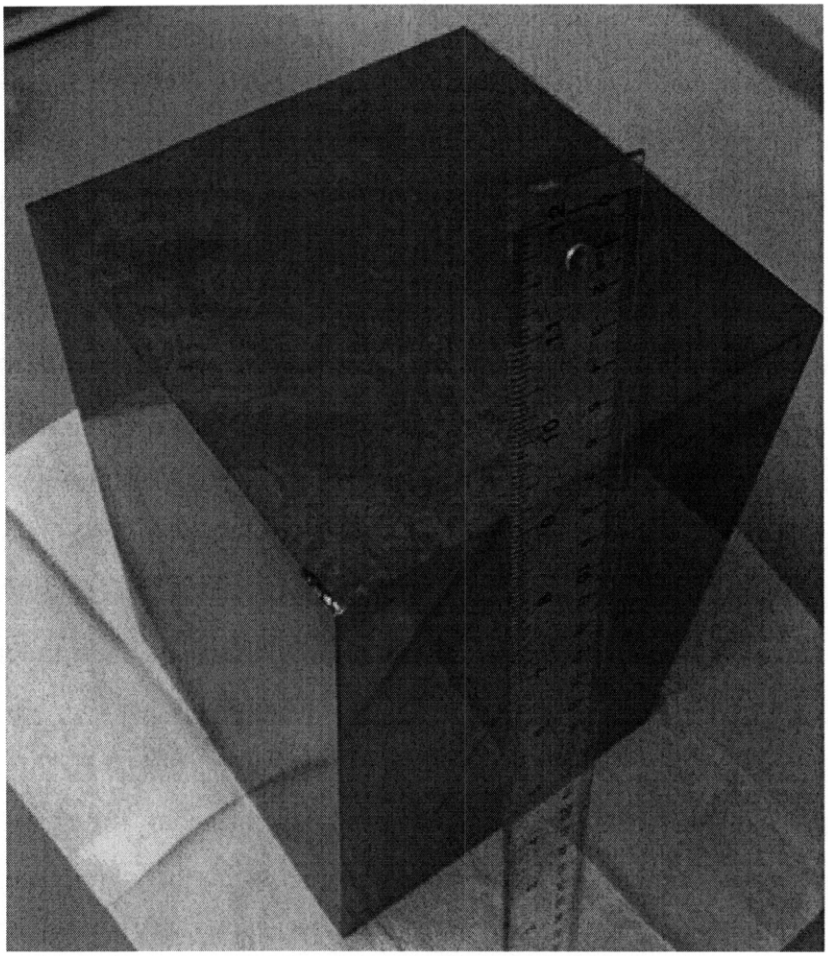

Figure 1.6: Cast multicrystalline silicon brick formed by directional solidification. Photograph of a brick sawed from a directionally solidified mc-Si ingot. The grain structure is visible on the top surface of the ingot.

After the ingot is created by directional solidification, it is sawed into vertical "bricks," one of which is shown in Figure 1.6. The bricks are then wire-sawed into wafers approximately 180 μm thick. Due to the finite thickness of the wire saw, as much as 50% of the silicon used in creating the ingot can be wasted as "saw dust," known as "kerf loss." After sawing, the wafers are chemically etched to remove damage from sawing. At this point, wafers can also be textured to encourage light-trapping [14].

Next, the pn junction is created by diffusing dopant atoms of the opposite type (e.g. n-type dopants into a p-type substrate) into the near-surface layer of the wafer. This is typically done using a $POCl_3$ gaseous-phase precursor that is deposited at high temperature onto the wafer, forming a "phosphorous glass" on the surface. The wafer is then and annealed at ~850-900°C for ~30 minutes, causing P to diffuse into the wafer and create a pn junction. The phosphorous

diffusion step can also help to purify the wafer, via external gettering. Because the deposited P-bearing layer on the surface of the wafer has a higher solubility for many impurities (such as Fe, Cu, and Ni), and because these elements are mobile at high temperatures (e.g. the diffusion lengths for Fe atoms at 850°C for 30 min is ~850 μm,[15]), a net diffusion of impurities from the wafer into the P-bearing surface layer can result [16].

After the remaining phosphorous glass is removed via chemical etch, an antireflection coating is deposited onto the wafer. A typical process consists of the deposition of silicon nitride (SiN_x) via plasma-enhanced chemical vapor deposition (PECVD) at approximately 450°C. This layer can also serve two additional purposes. Firstly, it can act as a surface passivation layer, by terminating dangling Si bonds present at the surface of the solar cell, which create mid-bandgap defect levels and reduce the effective lifetime of the wafer [17]. And second, if the SiN_x layer is deposited at the correct stoichiometry to be hydrogen rich, a subsequent high temperature anneal can diffuse hydrogen into the wafer, which has a similar passivating effect on several different types of defects, by passivating dangling bonds at internal defects [18-21].

Next, metal contacts are created, first by applying the metal (often by screen-printing), and then firing at high temperature to create ohmic contacts with the wafer. The back of the solar cell is typically metalized with aluminum, which provides the added benefit of creating a back-surface field that prevents diffusion of minority carriers to the back surface of the solar cell. Front metallization contacts are made from highly conductive metal (traditionally silver). This completes the production of the solar cell; further processing is required to create a module by series-parallel wiring of solar cells into a module. Figure 1.7 shows a small segment (~ 1x1 in^2) of an ingot-cast multicrystalline silicon solar cell.

Figure 1.7: Portion of a multicrystalline silicon solar cell.
The portion of a mc-Si solar cell shown above has been processed as described in section 1.2.3.1. The individual grains of silicon are evident. The white/silver lines are the solar cell metallization, where photo-generated current is collected.

1.2.3.2 Thin Film and Other PV Technologies

While crystalline silicon solar cells are a well-developed technology, much current work also focuses on the development of other PV technologies. The most-developed of these technologies is inorganic thin film photovoltaics. First Solar, the largest producer of thin film solar modules, uses CdTe as the semiconducting material. Other companies employ amorphous silicon (a-Si), copper indium gallium selenide (CIGS), and other materials. Thin film photovoltaics are called such because they are direct bandgap materials (i.e. electron excitation requires only a photon, as opposed to indirect bandgap materials that require a photon and phonon for electron excitation). As such, they can absorb sunlight in a much smaller thickness of material. The primary advantage of thin films is that they require much less material (as much as 100 times less active semiconductor material) than crystalline silicon solar cells, leading to materials cost reduction. Because of their thinness, they can also be adapted to flexible substrates, enabling "roll-to-roll" continuous processing, and providing further cost advantages over the batched processing of crystalline silicon.

Their primary weaknesses of current thin film photovoltaics are twofold: low efficiency and use of "exotic" materials. Commercially available thin film modules have overall energy

conversion efficiencies of less than 10%, compared with typical conversion efficiencies of 14-20% for various crystalline silicon technologies. Lower efficiency directly increases system costs of the technology.

Second, for the main thin film technologies in use today, the choice of materials presents problems for the long-term sustainability of each technology. For example, CdTe utilizes tellurium, of which the worldwide supply is estimated (using current annual production of tellurium) at an equivalent annual PV production of ~50-100 GW/year [22]. Other current technologies face similar challenges related to the abundance and extraction-cost of the active materials used [22]. Work is ongoing to develop technologies employing earth-abundant materials for use in low-cost, high efficiency inorganic thin film solar cells.

Other technologies currently under development include organic photovoltaics [23], dye-sensitized solar cells [24], and nano-engineered devices [25,26]. While these technologies potentially offer a combination of (very) high efficiency and/or low cost, they are still in the early stages of development, and are far from being commercialized.

1.2.4 Economics of PV

In order to be adapted at large scale, electricity from PV must compete with electricity produced by burning coal and other conventional energy sources. Thus, the primary goal of research in PV is to reduce the total cost of a PV system. One typical cost metric is cost per peak watt of capacity (where a peak watt is the size of a system needed to produce 1 W of power under "1 sun" illumination, or 1000 W/m^2 from the solar spectrum). Neglecting more complex cost issues (such as inverter cost, interest rates, capital depreciation, etc.), the total cost can be roughly approximated as follows:

$$Total\ Cost\left[\frac{\$}{W_p}\right] = \frac{Materials\ Cost\left[\frac{\$}{m^2}\right]}{\Phi\left[\frac{W}{m^2}\right] \bullet \eta[\%] \bullet Y[\%]} \tag{1.1}$$

η is the energy conversion efficiency, Y is the manufacturing yield, and Φ is a constant denoting 1 sun insolation. Thus, total system cost can be decreased by reducing the materials cost, increasing energy conversion efficiency, or increasing manufacturing yield.

It is also instructive to consider the history of photovoltaics to understand the market dynamics of the industry. Figure 1.8 shows the cumulative worldwide installed PV since 1992 [27]. Annual PV production has grown with an annual growth rate approaching 40% during this time period.

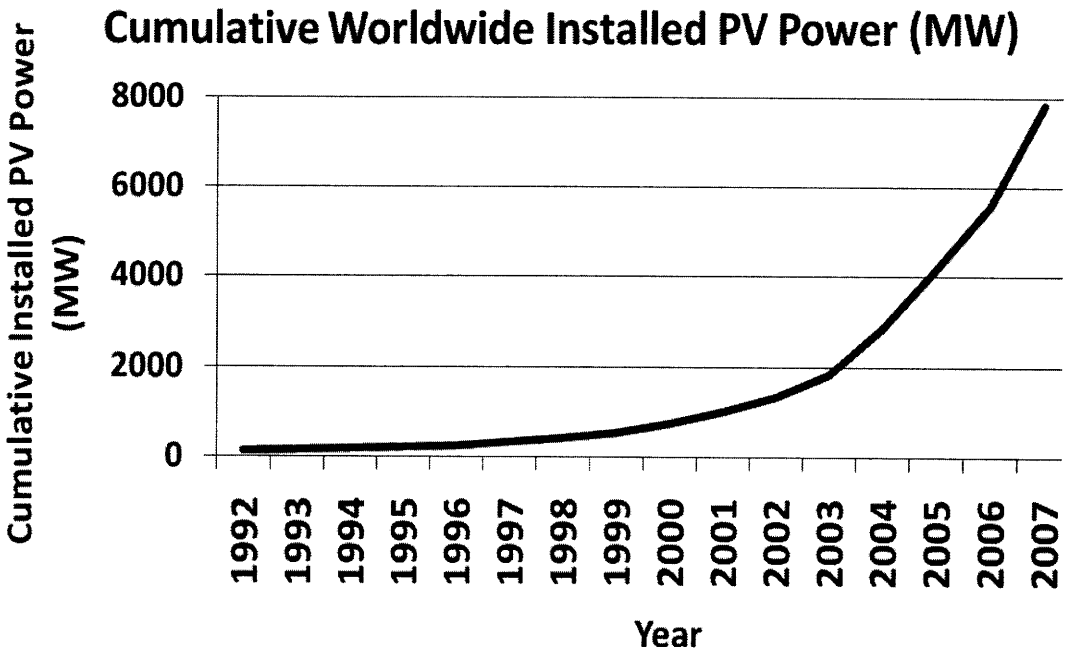

Figure 1.8: Cumulative worldwide solar cell production.
Data are from [27].

The bulk of this growth has been driven by (a good review of the history of PV technology market share is given in [28]). Motivated by this history, crystalline silicon is chosen as an area in which research can have an immediate impact upon a large manufacturing base. However, in order to enable widespread adoption of crystalline silicon PV, significant work is still needed to reduce cost and improve performance.

1.3 Defects in Crystalline Silicon

As evidenced in Equation (1.1), in order to lower the overall cost of photovoltaics, one can take three approaches (lowering materials costs, increasing efficiency, increasing yield). However, use of lower cost materials cannot be accompanied by such a reduction in efficiency as to offset the overall cost reductions. The focus of my work is to further investigation into various

defects in crystalline silicon, with the goal of enabling improvement of the performance of low-cost materials, such that they can perform as well as solar cells produced from current "high quality" material.

1.3.1 Minority Carrier Lifetime

One often-used measure of the quality of electronic material, and solar cell material in particular, is the minority carrier lifetime. After electron-hole pairs are generated (as seen in Figure 1.4), the minority carrier has a finite lifetime (on the order of 1-100 μs) before it recombines (i.e. the electron returns to the valence band). During this excited lifetime, the minority carrier (in p-type silicon, the electron) must diffuse from where it was created to the pn junction in order for charge separation to occur. The distance a minority carrier (in this case, an electron) can travel (diffusion length, L_e) is dictated by its lifetime (τ_e) and its diffusivity (D_e), as shown below:

$$L_e = \sqrt{D_e \tau_e} \tag{1.2}$$

As a result of this relationship, increasing the minority carrier lifetime leads directly to an increase in cell efficiency up to the point where diffusion length is much greater than the device thickness, at which point other factors begin to dominate. A more complete derivation of the relationship between minority carrier lifetime and cell efficiency is given in [29]. The effect of minority carrier lifetime is shown in Figure 1.9, calculated using the one dimensional solar cell simulation PC1D [30].

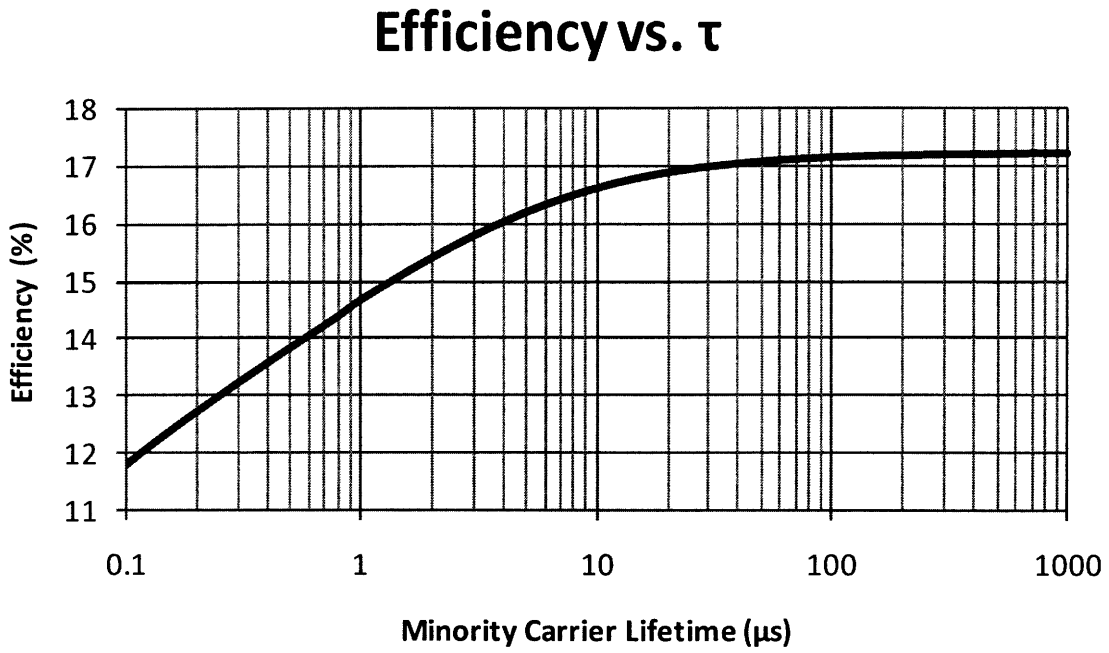

Figure 1.9: Dependence of efficiency on minority carrier lifetime.
For a solar cell modeled in PC1D [30] (230 μm thick p-type Si wafer), minority carrier lifetime is seen to have a large effect on cell efficiency up to 100 μs, beyond which other cell parameters begin to dominate.

The total effective lifetime can be calculated as the contribution of the lifetimes due to various processes and defects, according to the following equation.

$$\frac{1}{\tau_{eff}} = \frac{1}{\tau_1} + \frac{1}{\tau_2} + \ldots + \frac{1}{\tau_n} \tag{1.3}$$

τ_{eff} is the effective lifetime of the sample, and τ_1, τ_2, etc. are lifetimes due to different processes, such as radiative recombination (wherein a hole-electron pair recombines by emission of a photon) and Auger recombination (whereby the energy of recombination is imparted to a third carrier) [29]. Because of the form of Equation (1.3), the lowest lifetime tends to dominate the effective lifetime. Below, some of the most prominent lifetime-degrading defects are discussed.

1.3.2 Extended Defects

Extended defects in crystalline silicon are one- or two-dimensional deviations from the perfect diamond-cubic crystal structure of silicon. One-dimensional (line) defects are dislocations, which can generally be classified as edge dislocations or screw dislocations, or some intermediate combination. Two-dimensional (planar) bulk defects are grain boundaries. Because of the disruption of the local crystal structure and the resulting presence of dangling silicon bonds, allowed energy levels can be created within the bandgap, acting as recombination centers and decreasing minority carrier lifetime. Both the presence of crystallographic defects, as well as the interaction of these defects with various impurities [18,31-33], can be efficiency-limiting defects in crystalline silicon solar cells.

1.3.3 Impurities

Impurities in silicon can either be present as dissolved species (i.e. point defects) or clusters, such as precipitates or inclusions. While the presence of many impurities, including carbon, oxygen, boron, and phosphorous can all negatively impact solar cell performance, often the worst effects are observed from contamination of transition-metal impurities. As evident in Figure 1.10, this is in large part due to the high abundance of several key transition metals, especially iron, in the natural environment.

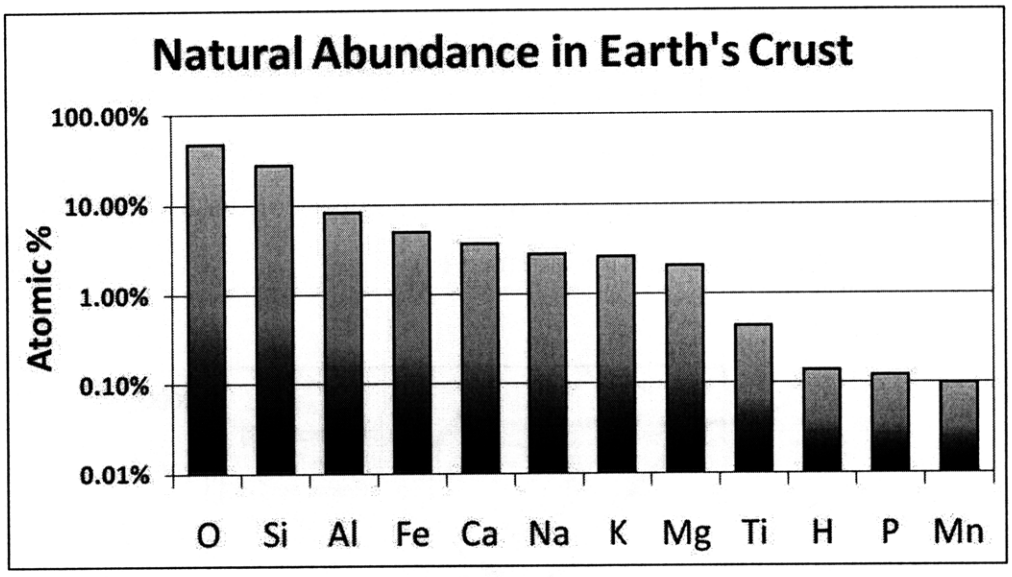

Figure 1.10: Natural abundance of the elements.

The 12 most abundant elements within the crust of the earth. Of interest is that silicon, the basis for > 90% of today's PV production, is the second most abundant element. Elements that are detrimental to PV performance, including Fe, Ti, and Mn, are also abundant. Data are from [34].

1.3.3.1 Dissolved Metals

Metals that are present as dissolved point defects are found to have a harmful impact on minority carrier lifetime [35]. There are several factors that determine how detrimental different metals are when present as dissolved species. Chief among these are the diffusivity and solubility of the metal. Metals with very low solubilities typically are not present in high enough quantities to significantly impact device performance. The diffusivity of metal species is also crucial in determining their impact, as it plays a large role in determining how "easily" each metal can be removed by processing and defect engineering. In solar cell processing, the competing effects of solubility and diffusivity can dictate an optimal temperature for removal of metals. Solubility-driven gettering (internal or external) occurs at lower temperatures due to supersaturation, whereas diffusivity is enhanced at higher temperatures [36]. For crystalline silicon solar cells, the optimal temperature for reducing dissolved iron content has been found to be between 400 and 700°C, depending on other factors such as the presence or absence of an external gettering layer [37,38].

Finally, the capture cross-section and defect level(s) of each metal determine how efficiently it can capture and recombine minority carriers [39]. Because of its combination of relatively high solubility, low diffusivity, large capture cross-section, and deep defect level, dissolved iron in the interstitial form (Fe_i) is often one of the most detrimental impurities found in crystalline silicon solar cells. Figure 1.11 shows the impact of dissolved iron in two forms (FeB complex and Fe_i) on minority carrier lifetime [40].

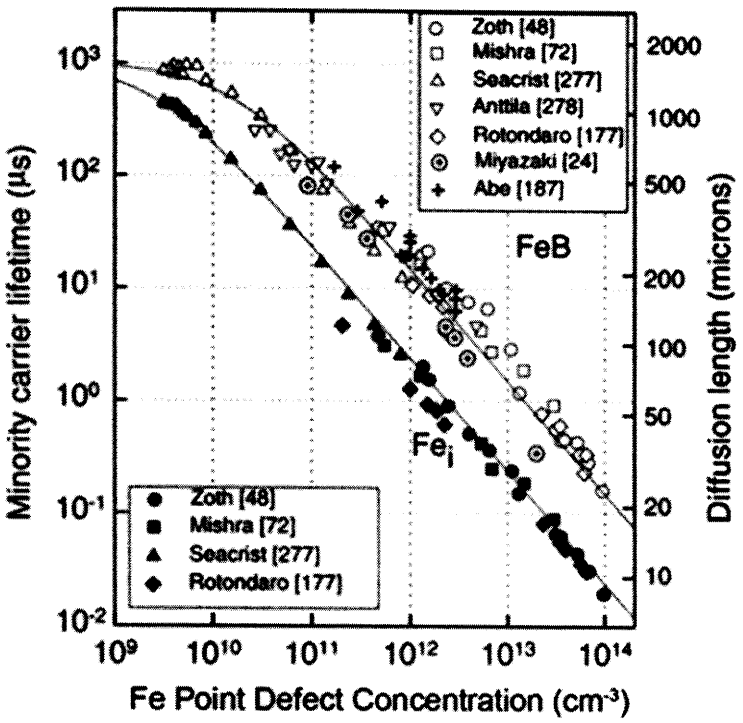

Figure 1.11: Impact of iron point defects on minority carrier lifetime.
Minority carrier lifetime as a function of Fe point defect concentration is plotted for both interstitial iron (Fe_i) and the iron-boron complex (FeB). Interstitial iron is observed to be more detrimental than the FeB complex. Figure from Ref. [40].

1.3.3.2 Precipitated Metals

Metals present in the form of precipitated particles (e.g. metal silicide particles) can also provide recombination pathways in crystalline silicon material [41]. However, while such precipitates can lower the performance of solar cells compared to "clean" material (i.e. material with much lower densities of metal impurities present as precipitates), the overall negative effect of metal precipitates is typically found to be much lower than that of metals in the form of dissolved point defects [42]. In fact, if metals that are present as dissolved point defects can be

induced to precipitate via thermal processing, material quality and device can be greatly improved [43].

Also of interest concerning the behavior of transition metals in crystalline silicon are the interactions between different metal species, as well as between these impurities and structural defects. In samples contaminated with multiple metals, precipitates are typically found to form as mixed-metal silicide precipitates [44,45]. Often, these precipitates are composed of multiple phases containing different compositions of metals (e.g. a Ni-rich precipitate with an adjacent Cu-rich "nodule"). In addition, the presence of grain boundaries and dislocations can greatly affect the precipitation of metal species by changing the energy barrier for nucleation and growth [46].

1.3.3.3 Other Impurities

While this work focuses on transition metal impurities, other types of impurities can have detrimental impacts on solar cell manufacturing and performance. For example, carbon, nitrogen, and oxygen present as precipitates can all reduce electrical performance [47-50]. Additionally, the unintentional presence of boron and phosphorous during liquid-phase refining steps can be particularly hard to mitigate, as the segregation coefficients of these elements are close to unity (i.e. they are not effectively removed during directional solidification) [11,51].

CHAPTER

2

HIGH TEMPERATURE X-RAY MICROPROBE TECHNIQUES

2.1 Introduction

In many materials systems of technological importance today, physical processes of interest occur at elevated temperatures, in the range of 100°C to 2000°C. This is particularly true in the field of energy conversion. For example, the conversion of chemical to electrical energy through the operation of solid oxide fuel cells can involve temperatures above 1000°C [52,53], and the catalytic reforming of methane into hydrogen and syngas can occur at temperatures above 1700°C [54,55]. As discussed in Chapter 1, in order to engineer desired bulk material and device properties, crystalline silicon solar cells are subject to high temperatures [56,17] during crystallization (above 1400°C), emitter diffusion (~ 850°C), annealing of antireflection coatings (~450°C), and metallization firing (up to 900°C). Underlying the changes in material properties at high temperatures are chemical and structural interactions at the micrometer and nanometer scales. To understand these phenomena, high resolution (better than 5 μm), high elemental sensitivity (better than 100 ppm) measurements are needed at variable temperatures under controlled ambient atmosphere.

X-ray fluorescence microscopy (μ-XRF), with variable spot size ranging from micron [57,58] to below 100 nm [59,60], probes large volumes of material within a short period of time, providing high resolution maps of nanometer-scale features. μ-XRF can provide orders of magnitude higher bulk sensitivity than transmission techniques based on X-ray absorption contrast [61]. Coupled with X-ray absorption microspectroscopy (μ-XAS) for determination of the chemical states of trace elements, μ-XRF is an ideal tool for investigating elemental and

chemical properties of bulk materials at the micron to sub-micron scale. For instance, μ-XRF and μ-XAS have been combined to shed light on performance-reducing metal impurities in crystalline silicon solar cell devices and precursor materials [62,63,42].

Extending these techniques to high temperature regimes will permit detailed study of bulk defect thermodynamics and kinetics, at the sub-micron scale. For instance, *in situ* high temperature X-ray microprobe investigations could elucidate how microscopic defects in solar cell materials respond to high temperatures typical of device manufacturing, enabling the development of defect engineering techniques that either seek to remove impurities from the material or otherwise minimize their electrical impact on the device.

Several synchrotron-based *in situ* X-ray techniques have been previously reported, but none of these incorporates all of the experimental parameters required for the successful study of high temperature microscopic phenomena in bulk materials. Studies have been presented of *in situ* X-ray microprobe experiments up to ~500°C [64-66], observing the behavior of Cu in fluid inclusions in quartz. However, the upper temperature limit of 500°C and the inability to the control ambient atmosphere limit its extension to our research. High temperature bulk XAS studies (1 mm spot size) on metal alloys and minerals at very high temperatures (up to 3000°C) were achieved [67-70], but they lacked the high spatial resolution required to study microscopic phenomena. High temperature and pressure studies [71] using diamond anvil cells have also been reported, but their use is limited to bulk powder and homogeneous liquid samples. Finally, scanning transmission X-ray microscopy has also allowed *in situ* spectromicroscopic studies of samples using soft X-rays [72]. However, these studies are limited to very thin samples (less than ~10 μm), and temperatures below 500°C. In addition to these synchrotron-based X-ray techniques, *in situ* electron microscope capabilities have been described for measuring samples at high temperatures (up to 1200°C) and under various atmospheric conditions [73-75]. While these techniques can perform controlled-ambient high temperature measurements, none can provide both high resolution and high sensitivity measurements over large volumes of material.

Herein is described the development of a stable, calibrated high temperature sample stage capable of measuring "bulk" materials (square millimetres in area, tens to hundreds of microns deep) at temperatures above 1200°C using microfocused hard X-rays. This has been accomplished while controlling the ambient atmosphere and minimizing thermal drift. I also present the first applications of the *in situ* high temperature sample stage to studying defects in

crystalline silicon solar cell materials at realistic processing temperatures, and further posit that the technique is well suited to study many of other material systems.

2.2 Technical Characteristics

2.2.1 Design Constraints

To enable experimental studies of a wide range of materials systems, temperatures in the range of 25 to 1200°C are desired. For kinetics studies, temperature accuracy, repeatability, and spatial homogeneity within the sample are required. Fast heating and cooling rates are also needed to study non-equilibrium systems and phenomena.

In order to integrate any high temperature device with the geometry of the XY sample stages at the beamlines used (ALS Beamline 10.3.2 [76] and APS Beamline 2-ID-D [77]), the sample must be oriented vertically (i.e. sample surface is perpendicular to incoming beam). Thus, a sample clamp must be employed to hold the sample in a vertical plane. Material selection of the clamp required consideration of the operating temperature and ambient gas in the chamber, as well as the avoidance of contamination of the sample or stage.

While physical processes often occur on the nanometer to micrometer length scales, many systems also exhibit millimeter-scale variations in properties. To effectively study samples exhibiting such spatial heterogeneity, the *in situ* sample heating stage for microprobe beamlines should accommodate samples up to several millimeters in size. In addition, the interaction of surface and bulk phenomena necessitates accommodating samples that are up to one millimeter thick. Additionally, to perform spectromicroscopy on the micron to sub-micron level, stability of the *in situ* sample heating stage is critical. Both microscopic vibration and macroscopic thermal drift must be minimized to enable characterization of materials over wide temperature ranges with high resolution.

In addition to temperature, control of the ambient atmosphere is needed, both for studying solid-vapor interfacial reactions, and for preventing undesired reactions such as oxidation. However, care must be taken to ensure the compatibility of the ambient gasses with the components of the high temperature sample stage itself. One example of material incompatibility is the exothermic eutectic reaction between Pt/Rh thermocouples and silicon samples at high temperature in a reducing ambient (e.g. 95% N_2, 5% H_2). Any window material

chosen to isolate and maintain the ambient atmosphere must transmit both incoming and outgoing X-rays without significantly diminishing signal due to attenuation or increasing noise due to high background impurity levels.

2.2.2 Implementation

2.2.2.1 Sample Stage

To enable studies such as described above, a commercially available Linkam TS1500 high temperature microscope stage has been modified (McCrone Group, Westmont, IL, USA, 60559), shown in Figure 2.1. This stage was chosen because of its integrated temperature control and compact size.

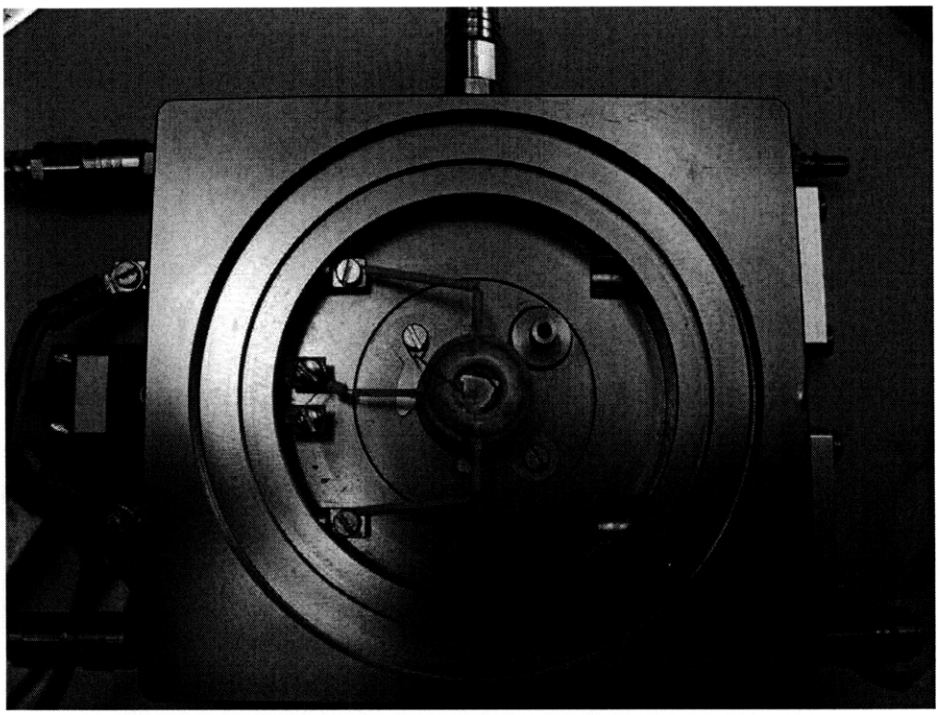

Figure 2.1: Linkam high temperature sample stage.
Photograph of the Linkam high temperature sample stage, without window.

Figure 2.2(*a*) shows a cross section diagram of a sample inside the sample holder. The sample sits inside a ceramic cup, which is heated conductively from the back via a resistive heating element comprised of a platinum wire, buried inside the ceramic. The aluminum body of the stage is water-cooled to below 50°C to reduce thermal drift and prevent damage to nearby components such as the fluorescence detector and incident beam ionization chamber. The water cooler is physically isolated from the sample stage to minimize water pump induced vibrations.

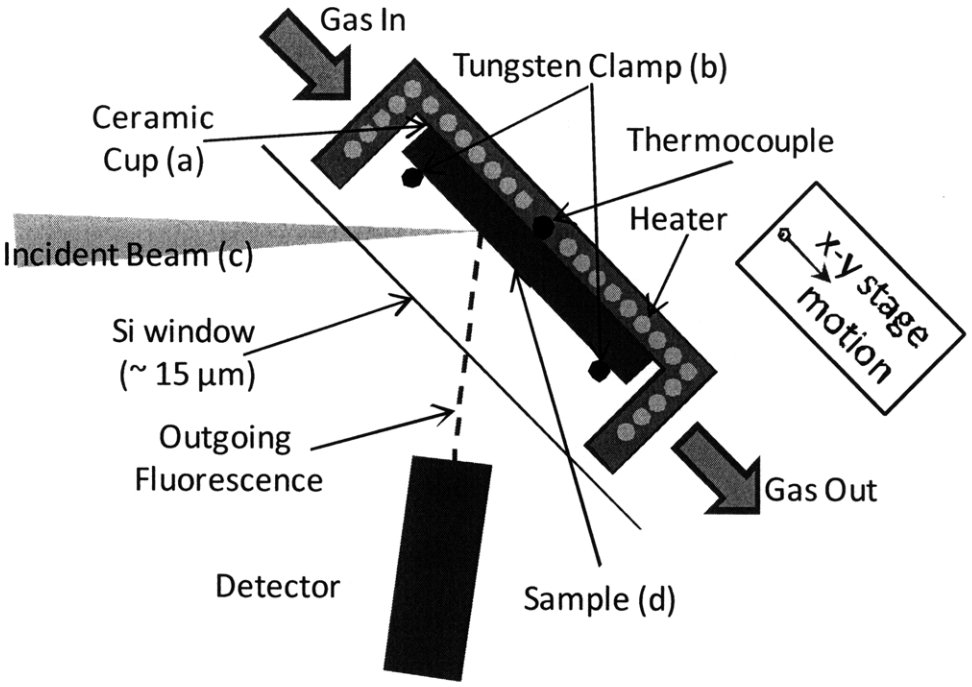

Figure 2.2: Schematic cross section of high temperature sample stage.
The sample is held in the vertical plane inside the ceramic cup. The cup is heated by buried platinum heating wires. Closed loop temperature control (Linkam TMS94 temperature controller) is provided via thermocouple feedback, and ambient atmosphere is controlled by flowing gas through the stage.

2.2.2.2 Sample Clamp

The sample is held in position by a tungsten wire (Figure 2.3, Figure 2.4); in this manner, sufficient pressure is maintained on the sample to ensure good thermal contact with the ceramic cup, minimizing the temperature drop due to thermal contact resistance.

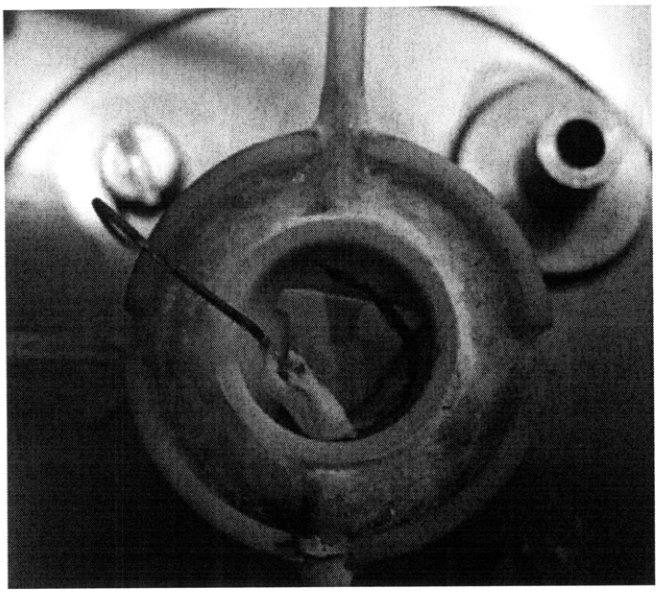

Figure 2.3: Silicon sample mounted in hot stage.
A sample of multicrystalline silicon is mounted inside the ceramic cup. It is held in place by a tungsten wire. A small piece of titanium wire is attached with high-temperature cement (Omegabond 600). Titanium, which has a very high affinity for oxygen, acts to getter any oxygen away from the sample, preventing oxidation of metals inside the silicon.

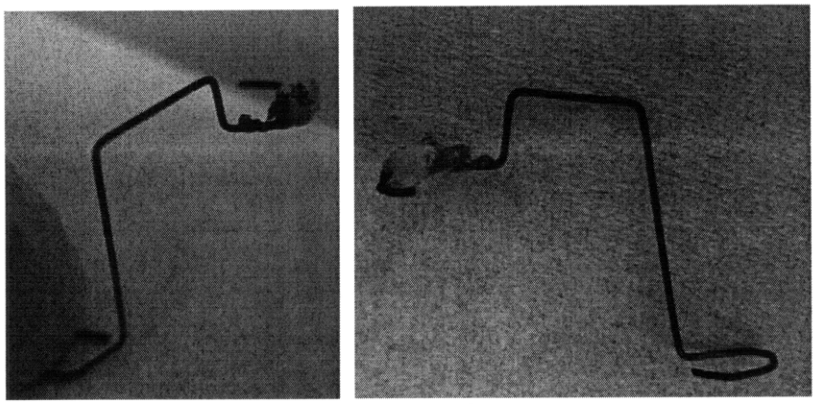

Figure 2.4: Tungsten wire clamp.
A piece of high-purity tungsten wire is bent into a clamp to hold the sample in the sample stage in the vertical configuration.

2.2.2.3 Window

A thin silicon wafer, approximately 15 ± 5 μm, commercially available from Virginia Semiconductor, Inc., is used to contain ambient atmosphere. The window was designed to optimize transmission while ensuring minimal transition-metal background impurities. Selection criteria for the window material are discussed further in Section 2.2.2.6. In addition to the window itself, a window mount was designed (Figure 2.5). The mount is an annular aluminum disk, ~2mm thick, which is sealed to the lid of the stage using vacuum grease. The window itself is sealed to the Al disk using silicone vacuum grease. The lid has two slots milled on a vertical milling machine, which enable the stage to be positioned at Beamlines 10.3.2 and 2-ID-D such that the sample is within the beam focal plane.

Figure 2.5: High temperature stage mounted at Beamline 10-3-2.
A photograph of the high temperature stage mounted at Advanced Light Source Beamline 10.3.2 is shown. The silicon window is in position

2.2.2.4 Beamline Mounting

To adapt the Linkam heating stage to the existing beamline geometry, custom mounting hardware was built. Titanium was selected in order to accommodate the weight limit of the XY stages at the beamlines used. The choice of titanium also provides for a relatively low linear coefficient of thermal expansion (8.6×10^{-6} °C^{-1} at 22°C) compared to steel (17×10^{-6} °C^{-1} at 22°C) and aluminum (23×10^{-6} °C^{-1} at 22°C). Figure 2.2(*b*) and (*c*) show a photograph and sketch, respectively, of the Linkam stage mounted on the XY stage of Beamline 10.3.2 at the Advanced Light Source.

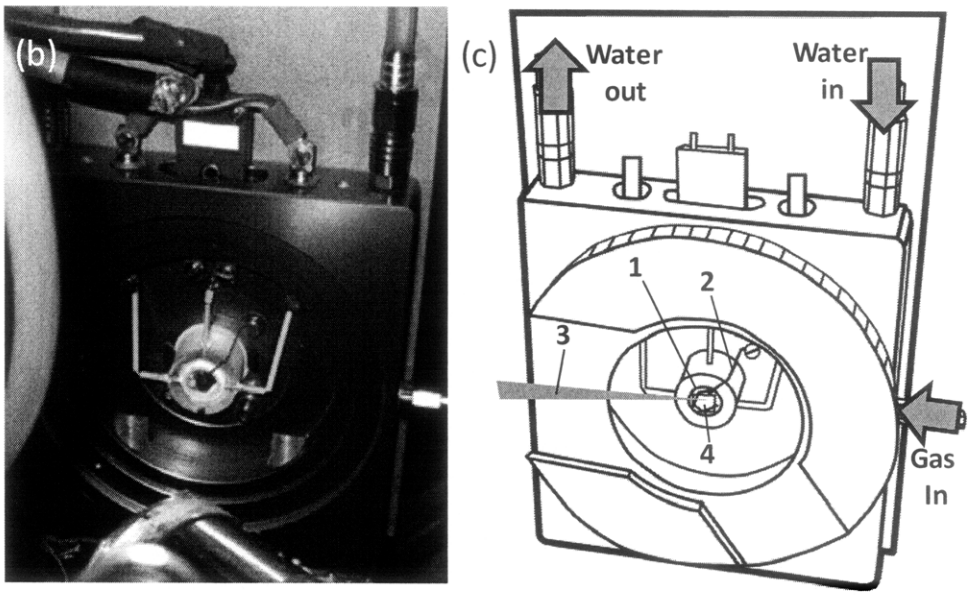

Figure 2.6: High temperature stage mounted at Beamline 10.3.2.
Photograph and sketch of the high temperature sample stage mounted at Advanced Light Source Beamline 10.3.2. Numbers in the diagram correspond to lettering in Figure 2.2. The sketch includes a screw-in window-mount, with slots used to accommodate placing the sample in the focus region of the beam.

For use in ALS Beamline 10.3.2, the Linkam stage is rotated such that the incident beam forms a 35° angle from normal to the sample. This constitutes a 10° CW rotation from the standard sample orientation of 45° with respect to the incident beam. Due to this rotation, as the sample stage travels in X, the beam spot on the sample surface increases due to slight loss of focus. The maximum increase of spot size is less than 10% over 8 mm of horizontal travel, for a beam divergence of 2 mrad and horizontal spot size of 2 μm.

Figure 2.7 shows the high temperature stage mounted at Advanced Photon Source Beamline 2-ID-D. A minimum spot size of 250 nm was measured by performing a line scan on a "knife-edge" sample of crystalline silicon with a thin layer of Cr. Spot size is measured as the FWHM of the resulting Gaussian curve along the line scan. The sample stage is oriented at 45° with respect to the incoming beam.

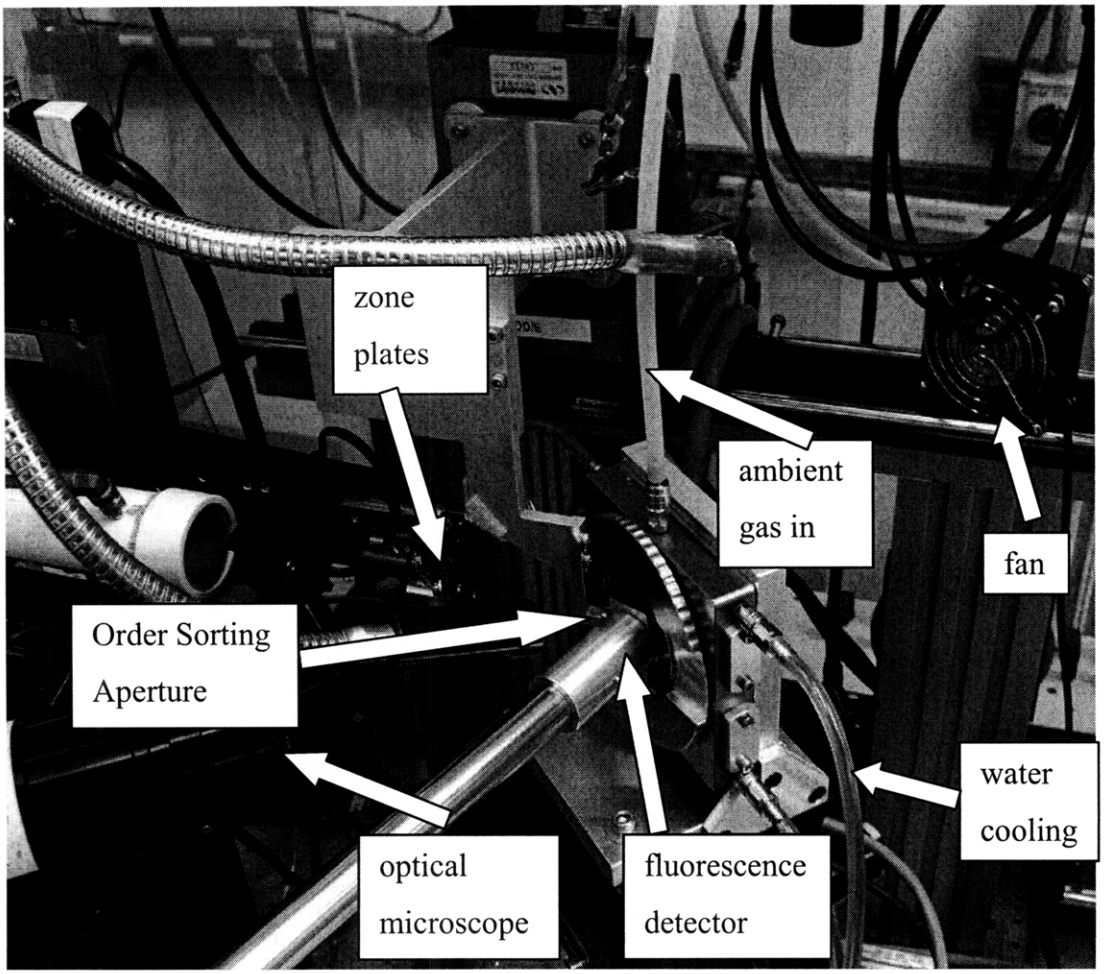

Figure 2.7: High temperature sample stage mounted at Beamline 2-ID-D.
A bird's-eye view is shown of the high temperature sample stage mounted at Advanced Photon Source Beamline 2-ID-D.

2.2.2.5 Software

The temperature of the high temperature stage is controlled using a closed-loop controller with thermocouple feedback. The temperature profile is remotely controlled using Linksys32 software commercially available with the Linkam TS1500 sample stage (screenshots shown in Figure 2.8).

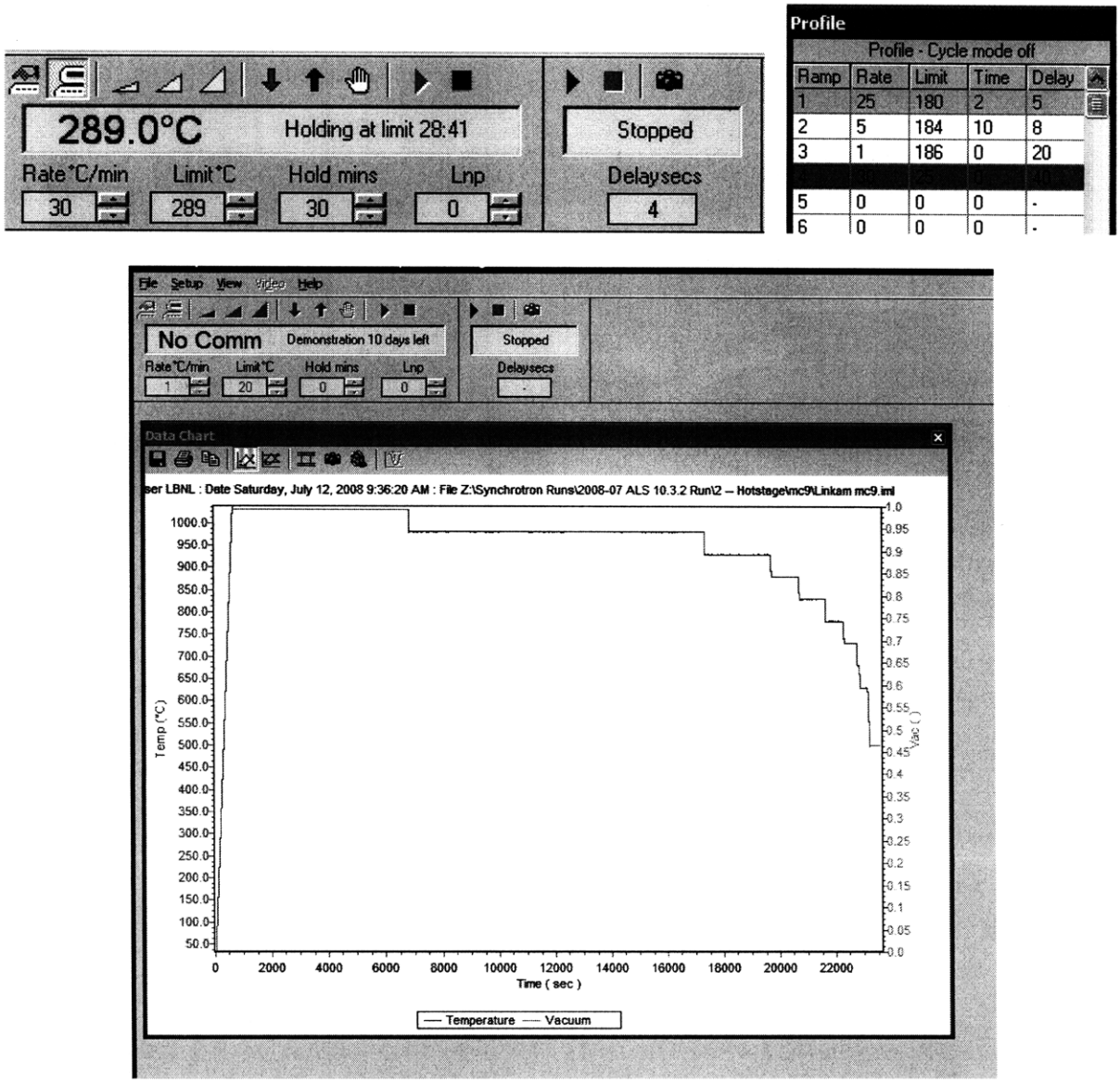

Figure 2.8: High temperature stage software.
Temperature profile was set and recorded automatically using the Linksys32 software package available with the Linkam TS1500 high temperature stage. Screenshots of the temperature control (top left), desired temperature profile (top right), and recorded data (bottom) are shown.

2.2.2.6 Ambient Gas

It bears noting that the gasses that can be used in the *in situ* sample stage are limited by several factors. Most important to consider is the compatibility of the sample stage equipment with the gas. Preliminary experiments were conducted using the sample stage in a reducing ambient of forming gas (~5% H_2, 95% (N_2 or Ar)), a non-flammable gas that is commonly used to prevent oxidation at high temperatures. This resulted in several failures of the system (shown in Figure 2.9 and Figure 2.10).

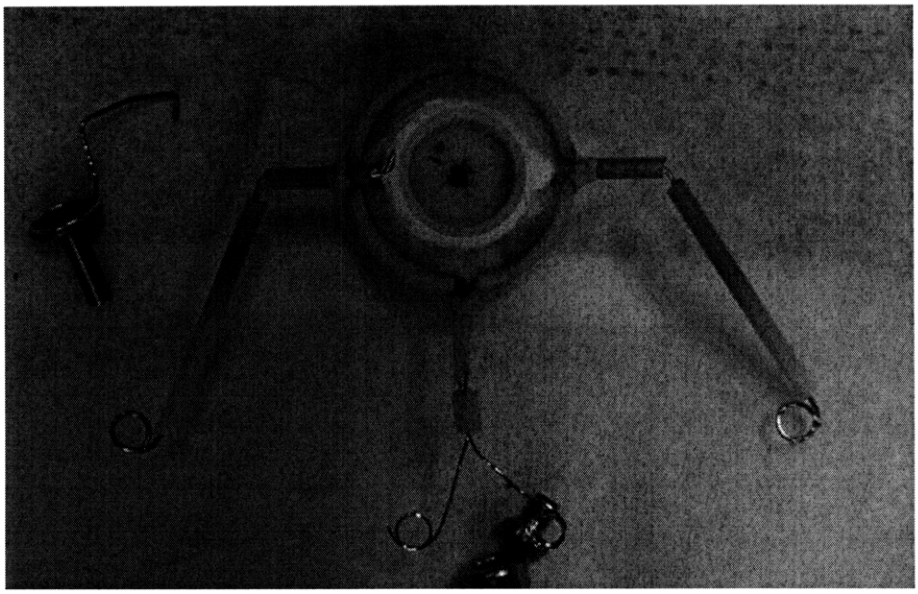

Figure 2.9: Ceramic cup after failure 1.
Photograph of ceramic cup and remains of platinum sample holder after first failure. The Si sample and Pt sample clamp formed a liquid eutectic droplet and destroyed the thermocouple inside the ceramic cup. This occurred under a forming gas ambient.

The first failure occurred when using a platinum (instead of tungsten) wire clamp to hold a crystalline silicon sample in place. The remains of the Pt wire clamp are shown in the left of Figure 2.9.

Figure 2.10: Ceramic cup after failure 2.
Photograph of ceramic cup after second failure. The Pt heater wire formed a liquid droplet with the silicon sample *through* the bottom of the ceramic cup (silver blob on bottom of ceramic in photograph). This incident also occurred in forming gas ambient.

The silver blob located roughly halfway between the outer and inner diameters of the ceramic cup in Figure 2.10 was the location of the second failure. In this case, a reaction occurred between the Pt heating wire and the silicon sample, again under a forming gas atmosphere.

2.2.3 Testing

The sample temperature was calibrated on the modified Linkam stage using three techniques: X-ray diffraction (XRD) to determine the lattice parameter of a crystalline sample as a function of temperature, optical pyrometry, and thermocouple thermometry. To measure the temperature using XRD, a sample of monocrystalline silicon grown in the [100] orientation was mounted inside a PANalytical X'Pert Pro X-ray diffractometer. Due to the physical constraints of the diffractometer, the high temperature sample stage was placed in a horizontal configuration for temperature calibration. As a result, the convection heat transfer condition was different for this measurement, contributing to experimental errors. From the measured lattice parameter as a function of nominal temperature, the actual temperature was calculated using the temperature-dependent coefficient of thermal expansion [78].

Temperature above 750°C was also calibrated using a Spectrodyne DFP2000 Disappearing Filament Pyrometer (DFP) [79,80], shown in Figure 2.11 and Figure 2.12. By matching the intensity of 650 nm radiation from the sample at high temperature with a calibrated, resistively heated wire inside the pyrometer, the temperature of the sample is determined. For this calibration, the silicon window must be replaced by a quartz window, because silicon is opaque to 650 nm radiation. The measurement relies on the spectral, temperature dependent emissivity of silicon [81].

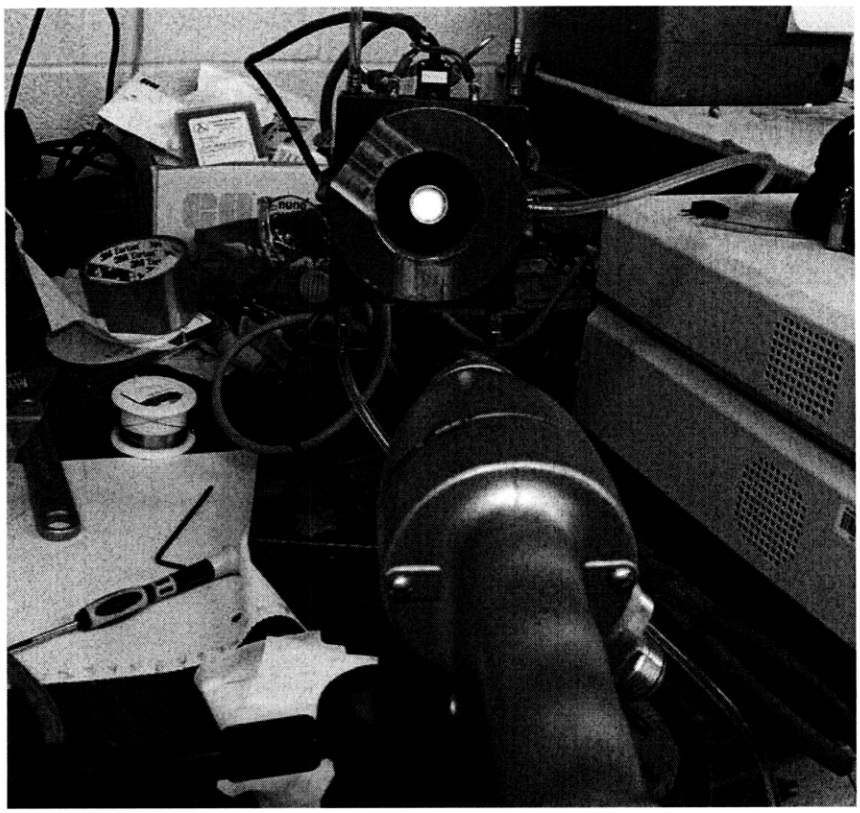

Figure 2.11: High temperature stage calibration via optical pyrometry.
The high temperature stage was heated in the vertical configuration, while being water cooled and with ambient gas being flowed in. The temperature was measured using the disappearing filament pyrometer mounted on a tripod for stability, pictured at bottom.

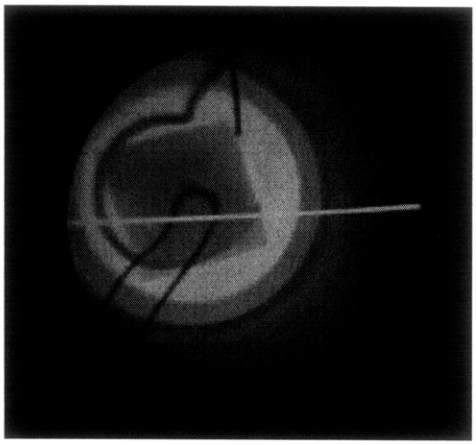

Figure 2.12: High temperature sample viewed through optical pyrometer.
A photograph taken through the optics of the optical pyrometer is shown. A knob on the pyrometer is turned, varying current through the filament seen above. When the correct current is achieved, the filament "disappears," and temperature can be read from the instrument. In the image shown, current (and thus filament temperature) is too high.

Finally, temperature was calibrated for the temperature range 25°C to 1200°C using a Type-S platinum-rhodium thermocouple. The thermocouple was cemented to a sample of multicrystalline silicon (Figure 2.13), and heated in the vertical configuration.

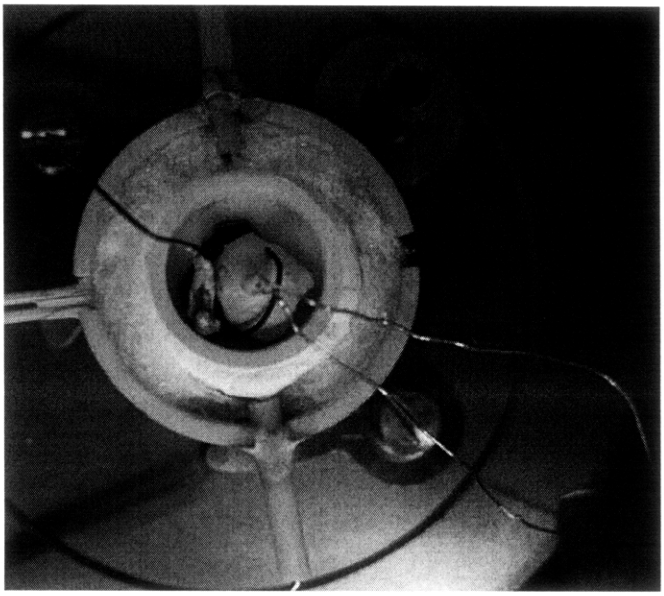

Figure 2.13: Thermocouple temperature calibration.
An S-type thermocouple cemented to a multicrystalline silicon sample is used for temperature calibration.

Figure 2.14 Figure 2 shows the temperature measurements and a linear fit, with slope 0.95. The overall variation of temperature measurements from the hot stage is determined to be

±8% of the measured value in Kelvins (i.e. 80 K at 1000 K). Approximately 75% of this error results from the thermal contact resistance between the sample and the heater, which varies widely as a function of contact pressure, surface termination, and roughness [82]. However, for a single sample, measured at different temperatures, the uncertainty of temperature differences is expected to be less than approximately 2%, because thermal contact resistance is unchanged between measurements, eliminating this source of variability.

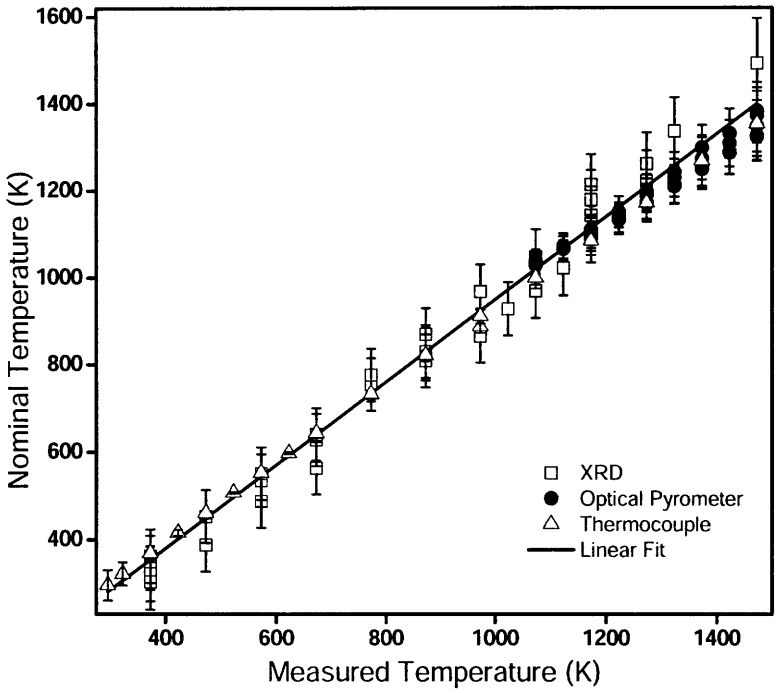

Figure 2.14: Temperature calibration of in situ sample stage.
Three calibration methods were used. Via X-ray diffraction, the lattice parameter of a monocrystalline silicon sample was measured, and the temperature calculated from the known coefficient of thermal expansion (squares). An optical disappearing filament pyrometer was used to measure the sample temperature (circles). A platinum-rhodium type S thermocouple cemented to a mc-Si sample was used to directly measure the temperature (triangles). The solid line is a linear regression to the temperature measurement data.

The window, which is necessary to control ambient atmosphere, must transmit both incoming and outgoing X-rays; thus transmitted signal is proportional to the product of ingoing and outgoing transmissivities. Figure 2.15(*a*) shows the theoretical transmissivity of various window materials [83] for two energies, representing typical values of incoming X-ray energy (10 keV) and outgoing fluorescence energy (~8 keV). While beryllium has higher X-ray

transmissivity, commercially available beryllium contains transition metal impurities in concentrations approaching $1x10^{19}$ cm^{-3}. This high level of impurities increases the noise level when measuring trace amounts of transition metals, reducing measurement sensitivity. Silicon was selected as the window material because of its combination of high X-ray transmissivity in the energies of interest, and sub parts-per-trillion background metal impurity content. In order to optimize overall transmission of X-rays, while maintaining sufficient mechanical strength to withstand operating conditions, windows of thickness of 15 ± 5 μm are chosen. μ-XRF maps taken without the window, Figure 2.15(*b*), and with the window, Figure 2.15(*c*), demonstrate the absorption losses due to the silicon window. 13% transmission of Ni-Kα signal is observed through the window. This lower-than-predicted transmission through the window likely results from shadowing of some portion of the fluorescence detector by the Al window mount; in future experiments, this artifact can be removed, and higher transmission values (approaching the predicted value of ~60%) can be expected.

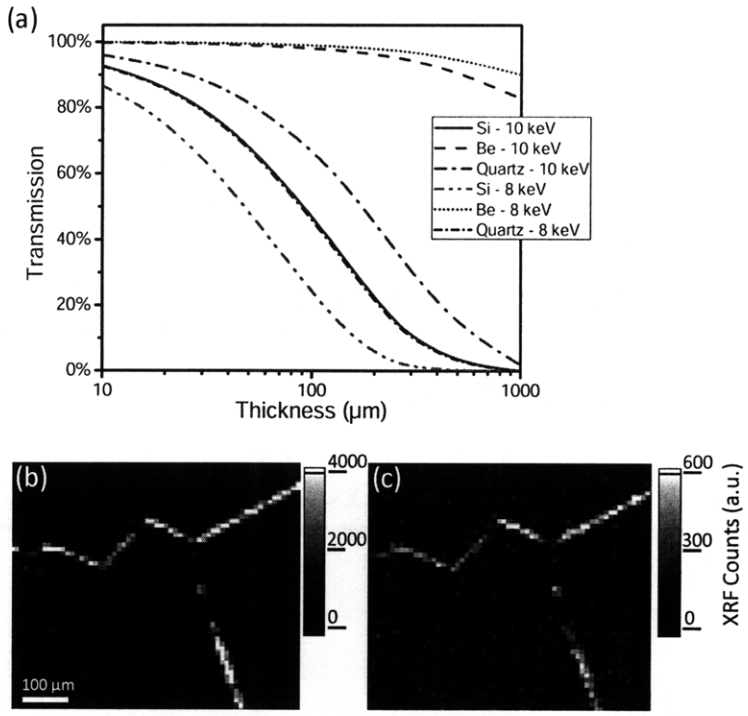

Figure 2.15: Selection and evaluation of window material.

(*a*) Theoretical transmission of Si, Be, and quartz windows as a function of thickness. (*b*) Ni Kα μ-XRF map of a metal-contaminated grain boundary inside the multicrystalline silicon sample, with no window. (*c*) Ni Kα μ-XRF map of the same grain boundary, with 15 ± 5 μm Si window. 13% transmission of Ni Kα signal is observed. Note the different intensity scales in the two images.

CHAPTER

3

HIGH TEMPERATURE STUDIES OF CRYSTALLINE SILICON SOLAR CELL MATERIALS

3.1 Introduction

The development of the new sample heating stage for X-ray microprobe discussed in Chapter 2 enabled experiments on crystalline silicon solar cell materials at high temperatures. As discussed in Chapter 1, silicon undergoes a series of high temperature processing steps ranging from <500°C to >1400°C. By investigating metal impurities in crystalline silicon under realistic processing conditions, we gain insight into the behavior of these impurities.

This chapter is divided into sections concerning different experiments. The first experiment on surface diffusion was designed to broadly test and verify the performance and capabilities of sample heating stage. The following experiments on metal-silicon liquid droplet formation and behavior elucidate the high-temperature thermodynamics and kinetics of crystalline silicon under solar cell processing conditions.

3.2 Methods and Materials

To test the hypothesis of retrograde melting in silicon, the X-ray microprobe sample heating stage whose development is discussed in Chapter 2 was used to investigate silicon samples contaminated with transition metals at high temperatures.

Solar cell material was obtained from industrial solar cell manufacturers in the form of as-grown cast multicrystalline silicon (mc-Si) wafers, 200 μm thick. 5x5 mm^2 squares were cut

from wafers (to fit within the high temperature sample stage) using a 1064 nm laser cutting and scribing tool. Figure 3.1 shows an example of such samples. The samples were then cleaned with acetone and ethanol to remove organic contamination, and then lightly etched in a solution of hydrofluoric, nitric, and acetic acids to remove any possible remaining surface contamination.

Figure 3.1: Laser-cut and marked samples.
A 1064 nm laser was used to cut samples into 5x5 mm^2 squares, and to scribe names into the samples. On the sample shown above, the center square was experimentally investigated using the high temperature *in situ* stage. The squares on either side were used to enable the sample to be clamped during deposition of thin metal films, for intentional contamination.

3.3 Surface Diffusion

A first experiment was planned to test the capabilities of the developed *in situ* sample heating stage, and to verify its ability to enable studies of crystalline silicon samples at high temperatures. To this end, we chose the phenomenon of surface diffusion as a suitable topic for a brief study. Surface diffusivity, a property that varies widely with surface preparation [84], is normally lower than bulk diffusivity [85], with an activation energy for surface diffusion that is roughly proportional to the bulk diffusion activation energy. In this study, we compare the surface diffusion of Cu, which has relatively high bulk diffusivity ($D_{Cu} = 4.7x10^{-5}$ cm^2 s^{-1} at 860°C), with that of Fe, which is more than an order of magnitude lower ($D_{Fe} = 1.0x10^{-6}$ cm^2 s^{-1} at 860°C).

In order to study surface diffusion of these transition metal species in silicon, a sample of multicrystalline silicon was prepared by scratching the surface with iron and copper wires. This

effectively "deposited" a thin layer (non-homogeneous) of the metals along the surface of the sample. The sample was heated rapidly (100°C/min) to 860°C in N_2 ambient atmosphere, and repeated samples scans were taken to map the distribution of metals as a function of time.

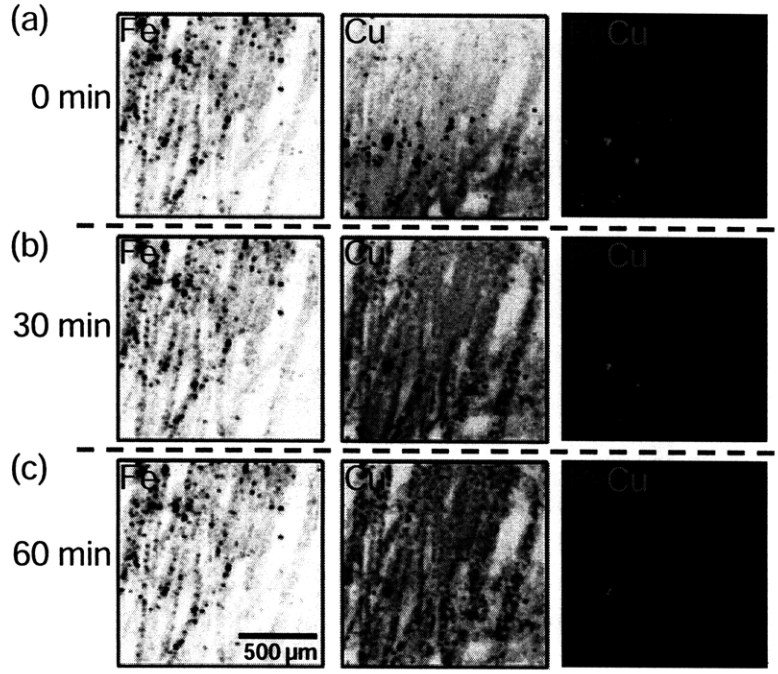

Figure 3.2: Surface diffusion of metals on mc-Si sample at 860°C.
µ-XRF elemental distribution maps of Fe-Kα, Cu-Kα, and Cu and Fe together, are shown after (*a*) 0 minutes, (*b*) 30 minutes, and (*c*) 60 minutes. Cu is seen to rapidly diffuse along the sample surface; Fe concentration changes due to surface diffusion are below the detection limits. Maps were collected at ALS Beamline 10.3.2 with pixel size of 10 x 10 μm^2.

Figure 3.2 shows high temperature elemental mapping analyses over the course of 60 minutes. The area of the sample mapped is approximately 1 x 1 mm^2, and each map took approximately 30 minutes. During 60 minutes of high temperature measurements, Cu diffused hundreds of microns along the surface of the sample. No Fe concentration variations are conclusively seen in this experiment, likely because they fall below the detection limit. Only small amounts of Cu diffuse between 30 and 60 minutes of heating, likely due to the Cu being in a near-equilibrium state after the first 30 minutes at high temperature.

The observation of Cu diffusing faster than Fe at 860° is in good agreement with their diffusivities being more than an order of magnitude different, and it confirms the ability of the *in situ* technique to dynamically map large sample areas as a function of time and temperature.

Ongoing work by others is currently using a similar setup to investigate other metal diffusion processes in multicrystalline silicon.

3.4 Measuring Liquid Metal-Silicon Droplets

To verify the existence of liquid metal-silicon droplets, and to quantify their XAS spectrum for identification in further experiments, extended X-ray absorption fine structure (EXAFS) spectroscopic measurements were performed on a specially prepared "standard" sample. Using e-beam evaporation, alternating layers of metal (320 nm $Ni_{0.8}Fe_{0.2}$, 300 nm Cu, 300 nm $Ni_{0.8}Fe_{0.2}$, 300 nm Cu) were deposited onto a wafer of cast mc-Si. This was then capped with a thin piece (<15 μm) of monocrystalline Czochralski Si (CZ-Si), as shown in Figure 3.3(*a*).

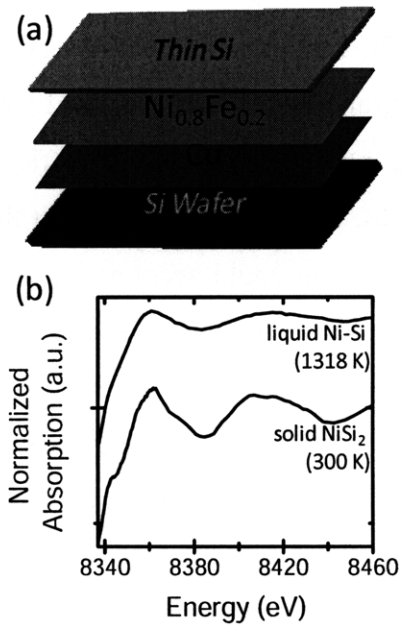

Figure 3.3: Measurement of liquid Ni-Si Ni-XANES.
(*a*) Nickel, iron and copper deposited between silicon wafers is heated above the eutectic temperature. (*b*) Ni K-edge XANES measurements at 1045°C on the resulting liquid metal silicide at 1045°C. The solid $NiSi_2$ spectrum is shown for comparison.

The sample was heated in N_2 ambient to 1045°C, above the Ni-Si and Cu-Si eutectic temperatures and the chemical state was determined using μ-XAS. Figure 3.3(*b*) shows the resulting X-ray absorption spectrum from the liquid sample. Extended X-ray absorption fine

structure (EXAFS) first-shell fitting out to k = 9.4 $Å^{-1}$ was performed using Artemis with FEFF6L [86]. The results suggest that the high temperature particle observed in Figure 3.3(*b*) has a smaller Ni-Si distance and reduced coordination number compared to $NiSi_2$. These spectroscopic observations are consistent with the existence of a liquid phase. In addition, visual inspection of the sample revealed that the Si cap layer was fused to the mc-Si substrate, and the previously continuous film had dewetted, suggesting the existence of a high temperature liquid state.

3.5 Retrograde Melting

3.5.1 Background

Retrograde melting, a counterintuitive phenomenon describing a solid-to-liquid phase transition *upon cooling* [87,88], has been reported under standard conditions only in a few metallic and organic systems [89]. The first experimental observation of retrograde melting in a semiconductor material is presented, and a pathway proposed for its occurrence. Liquid metal alloy droplets formed via retrograde melting are seen to be efficient sinks for the local internal gettering of dissolved metal impurities. Further, it is shown that the formation of liquid droplets on cooling and subsequent re-solidification could account for previous observations [90,91] of phase-segregated metal-silicide particles in multi-metal contaminated Si. These phenomena present a promising approach for manipulating impurities in semiconductor materials on the nanometer scale, potentially offering a means of improving the efficiency of low-cost solar cells by reducing the bulk concentration of dissolved impurities that act as recombination centers.

Understanding of impurities in semiconductors has proven of fundamental importance for engineering high performance devices [92]. Impurities directly affect the lifetime and mobility of carriers and thereby the performance of semiconductor material. Segregation gettering is one highly effective and widely implemented technique for purifying silicon and other semiconductor materials during crystal growth [93]. The solubility of impurities can be orders of magnitude higher in a liquid phase than in solid semiconductors. This differential solubility results in a driving force for impurity segregation to the liquid, and an effective cleansing of the crystalline solid [94]. Typically, solid-to-liquid impurity segregation occurs during the cooldown of molten silicon during a directional solidification step, for example during ingot growth of

multicrystalline silicon [95], or during the Czochralski method of growing monocrystalline silicon [96].

Herein, the formation of liquid droplets *within* solid silicon during an annealing process is observed, and it is hypothesized that their formation results from retrograde melting. Internal gettering of bulk metal impurities to these liquid droplets is also observed. Upon cooling, they form multiple metal alloy precipitates in the silicon. A theoretical pathway for the formation of these particles is proposed. Understanding of impurity precipitation, after crystal growth and during the processing, offers new possibilities for tailoring the structure of embedded nanoparticles in a range of semiconductor-based materials systems. Specifically, a theoretical model of precipitate formation during solar cell manufacturing is offered, which clarifies the formation mechanism of a common defect in multicrystalline silicon solar cell manufacturing, and suggests a path towards improving solar cell production and enhancing device performance.

The phenomenon of retrograde melting (in inorganic materials), whereby a liquid phase forms from a solid phase *upon cooling*, has been observed and studied in several systems, including Fe-Zr [97] and Mg-Fe-Si-O [89]. One common pathway for this process to occur is via the catatectic reaction, occurring at an invariant point on a binary phase diagram involving transformation from Solid → Solid + Liquid [98]. Many binary systems exhibit such an invariant point [99], including Ag-In, Cu-Sn, Fe-Mn, and Fe-S [100] but very few semiconducting materials possess a catatectic point [101]. Abrosimov proposed a second model for the formation of liquid droplets within a solid matrix material. In this model, locally-supersaturated impurities at a grain boundary are included directly from the melt during crystal growth [102]. The phenomenon observed in the present experiment cannot be explained by either of these pathways as the material does not possess a catatectic point, nor are the precipitates seen in the original crystalline material.

A third pathway for the formation of liquid droplets is proposed in systems, such as silicon, which exhibit the phenomenon of retrograde solubility. Due to the high enthalpy of formation for point defects, the solid solubility of a second species within the crystal structure increases with temperature, reaching a maximum well above the eutectic temperature. Most dissolved elements in silicon demonstrate this property [94], including the 3d transition metals such as iron, copper, and nickel [103]. It has been hypothesized that retrograde solubility can lead to the formation of liquid droplets upon cooling [91], if supersaturation occurs at a

temperature above the eutectic temperature, as demonstrated in Figure 3.4(a). However, up to this time, experimental verification has proven elusive.

3.5.2 Experimental

To test the hypothesis of retrograde melting in crystalline silicon, a sample was prepared containing high concentrations of transition metals (Fe, Ni, and Cu). A high-purity multicrystalline silicon (mc-Si) wafer was intentionally contaminated by first sputtering a thin layer of metals (3 nm Fe, 15 nm Ni, 35 nm Cu) onto the wafer. The sample was then annealed at 1,140 °C for 30 minutes before being quenched to room temperature. The resulting concentration of metals inside the wafer are given by the solubility limited concentrations of the metals at the annealing temperature ($2.7x10^{18}$ cm^{-3} Cu, $1.3x10^{18}$ cm^{-3} Ni, and $5.9x10^{15}$ cm^{-3} Fe) [103,15]. In addition, the Cu concentration is above the solubility limit at 802 °C, the Cu-Si eutectic temperature, satisfying the condition for retrograde melting and Cu-Si liquid droplet formation. The sample was quenched to trap high concentrations of dissolved metals within the bulk, and to prevent the dissolved metals from forming large precipitates or diffusing to the surface during cooling. The samples were cleaned in acetone and isopropanol to remove organic contamination, then hand-polished and chemical-etched to remove any remaining metals, oxides, or silicides from the sample surface, leaving only metals dissolved or precipitated in the bulk.

At Beamline 10.3.2 of the Advanced Light Source, the sample was then rapidly heated (100 °C min^{-1}) to 980 °C in the *in-situ* microprobe heating stage. A μ-XRF map of a grain boundary (GB) region, Figure 3.4(b) 980 °C, shows that no metal precipitates were present above the detection limits. To bring about retrograde melting, the sample was then cooled to 930 °C and remapped, exhibiting the formation of particles along the GB, Figure 3.4(c). The initial nucleation of the liquid droplets occurred at a lower temperature than the expected solidus temperature, likely because there was some out-diffusion of metals during quenching/cooldown and reheating (lowering total concentration of dissolved metals), and possibly due to a high nucleation energy barrier for Cu-rich precipitates [104]. A μ-XAS spectrum of the particles at the Ni K-edge was consistent with the short-range order of a liquid (Figure 3.4(c)), as described in Section 3.4.

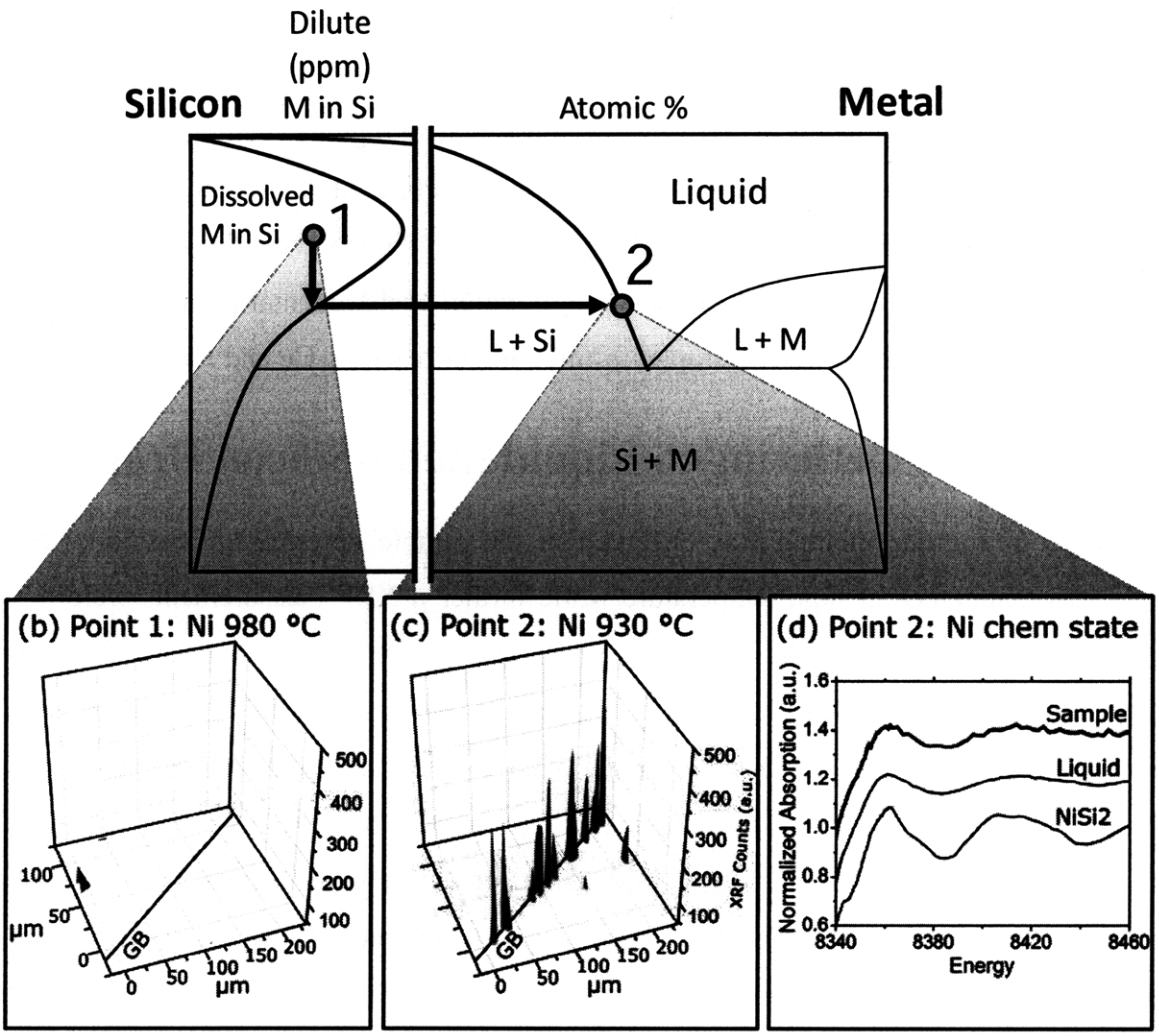

Figure 3.4: Formation of liquid droplets via retrograde melting.
(a) A schematic binary phase diagram for an M-Si system (where M is a 3d transition metal) demonstrates the pathway for formation of liquid droplets, resulting from the retrograde solubility of the metal in Si. (b,c) μ-XRF 3D maps of a grain boundary in mc-Si show no large particles at 980 °C and particles along the GB at 930 °C. (d) Ni K-edge μ-XAS reveals that the droplets are in the liquid state.

The formation of liquid droplets in mc-Si can be explained by examining the schematic phase diagram shown in Figure 3.4(a). The sample initially has a high concentration of dissolved metals within the silicon, and is rapidly heated to at a temperature above the eutectic temperature, in the region of retrograde solubility. As the sample is cooled, the liquidus is crossed, and liquid droplets form due to supersaturation. In other words, a melting reaction that occurs *while cooling*, i.e. retrograde melting.

Thus for the first time the phenomenon of retrograde melting is demonstrated in a semiconductor material. Additionally, for the first time, we demonstrate the occurrence of

retrograde melting due to retrograde solubility within a binary (or pseudo-binary) phase diagram. The importance of this discovery, as well as potential applications of this knowledge to solar cell processing are discussed below. Briefly, we propose that retrograde melting and the resulting liquid droplets could be used to encourage internal gettering of dissolved metal species (as discussed in Section 3.6). Another proposed application could be to avoid the formation of liquid droplets altogether, and thereby reduce total incorporation of detrimental impurities (e.g. Fe) by reducing the concentration of liquid-droplet forming impurities (e.g. Cu and Ni).

3.6 Internal Gettering to Liquid Metal-Silicon Droplets

After retrograde melting was observed in the sample described in Section 3.5.2, the sample was maintained at high temperature while further μ-XRF measurements were made of the liquid metal-silicon droplets along the GB. In Figure 3.5(a-f), successive elemental distribution maps of Cu and Fe along a GB are shown. Copper is present in higher concentration, in line with its higher bulk solubility in silicon [103]. Both Cu and Fe concentrations at the liquid droplets along the GB increase with time, indicating that these particles are growing by gettering dissolved metal species from the bulk. This is demonstrated in Figure 3.5(g) by the background-subtracted, normalized metal concentration plots. In order to determine relative concentrations of elements, XRF signal was spatially integrated to quantify the total counts of a given element. The particle described in Figure 3.5(g) was integrated with a 27 x 27 μm^2 box (chosen to include the entire particle during growth). The background level was subtracted by integrating a box of the same area from a region away from the grain boundary with no metal particles; the total counts of the particle were then reduced by this amount. Concentrations are given as relative quantities because during the experiment, no standard material was measured; thus, no absolute values for concentrations can be calculated. The final data point (t = 104 min) was selected for normalization so that the plot scaled to unity.

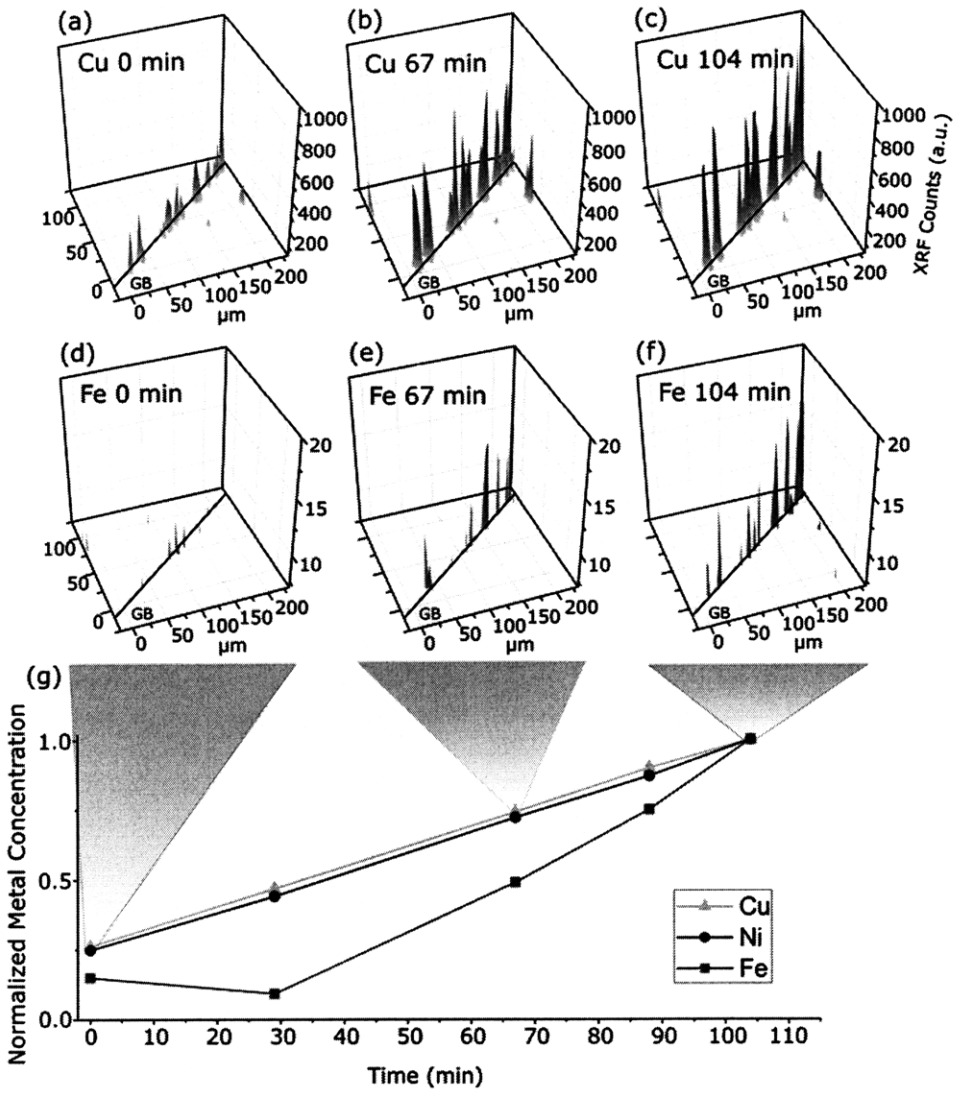

Figure 3.5: High temperature gettering of metals to liquid droplets.
(a-f) μ-XRF maps, shown in 3D, taken at 930°C. (a,d) Elemental distribution maps show the initial clustering of Cu precipitates along a grain boundary, with very small amounts of Fe. (b,e) After 67 minutes, both Cu and Fe precipitates have grown. (c,f) After 104 minutes, Cu and Fe particles continue to grow. (g) Concentration plots (normalized with respect to concentration at t = 104 min) of Cu, Ni, and Fe in a representative particle as a function of time show that Fe is effectively gettered to liquid droplets. μ-XANES measurements (not shown) confirm the liquid state of these droplets.

The μ-XRF counts of Cu and Ni are seen to grow linearly, consistent with a diffusion-limited growth process to a favorable non-solubility limited aggregation site (i.e. an "infinite sink"). Iron is also observed to accumulate at a linear rate, but the amount of iron in these particles grows more rapidly than copper or nickel. This iron accumulation in the liquid copper and nickel silicide droplets is consistent with a segregation gettering effect. This experiment thus

illustrates internal liquid gettering, and demonstrates one potential positive benefit of liquid metal-silicon droplets.

3.7 Metal Silicide Precipitate Solidification

As discussed in Chapter 1.3.3.2, metal silicide precipitates are a common defect in as-grown multicrystalline silicon wafers, especially in material taken near the top, bottom, and edges of ingots. These precipitates are often found to have morphologies of the type shown in Figure 3.6, consisting of separate phases with different elemental compositions. In the example shown, the precipitate is composed of a $NiSi_2$-like phase containing large amounts of Fe, and a Cu_3Si-like phase with a lower concentration of Fe.

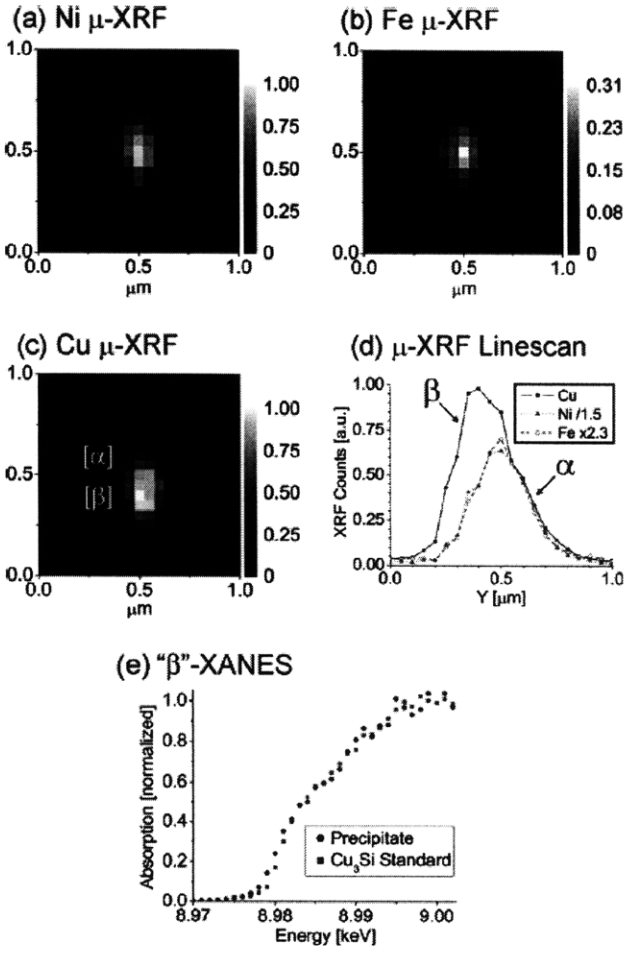

Figure 3.6: Distributions of Metals in As-Grown Silicon Sample.
Nickel and iron are observed to be co-located in the upper precipitate. Copper is concentrated in the lower "nodule." Figure reproduced from [44], with permission.

In order to develop a deeper understanding of the formation of such metal silicide precipitates, and to connect the observation of liquid metal silicide droplets with previous observations of mixed-metal silicides in the solid phase, the following experiment was performed. A sample was prepared by intentionally contaminating a mc-Si wafer with alternating layers of metal (320 nm $Ni_{0.8}Fe_{0.2}$, 300 nm Cu, 300 nm $Ni_{0.8}Fe_{0.2}$, 300 nm Cu) deposited by e-beam evaporation. The metal-coated side of the sample was then covered with another piece of mc-Si and annealed at 1,140 °C for ~30 minutes, cooled at a rate of ~5-30 °C s^{-1}, and quenched to room temperature (oil quench, ~100-200 °C s^{-1}). After quenching, the sample consisted of a "sandwich" of metals between two mc-Si wafers.

Cleaning in acetone removed any organic contaminants, and light hand polishing and subsequent chemical etch of hydrofluoric, nitric, and acetic acids in a ratio of 11:2:4 removed any metals that had diffused to the outer surfaces. This etch is slightly anisotropic, in order to reveal grain boundaries; high energy grain boundaries were selected as regions of interest for investigation.

The amount of metal deposited on each sample was much larger than the amount needed to saturate silicon at the annealing temperatures. Thus the concentration of metals in all samples was determined solely by the solubility of each metal at the annealing temperature.

The sample was heated to 1,080 °C for approximately 12 hours to allow formation, growth, and stabilization of liquid droplets at near-equilibrium conditions. To observe liquid droplet formation, the sample was then slowly cooled (1-3 °C min^{-1}), and characterized by *in-situ* μ-XRF/XAS during the cool-down. By taking repeated maps of a 100 x 100 μm^2 area while cooling, the spatial distribution of metals in a large liquid droplet was tracked. μ-XAS measurements taken after each μ-XRF map provide information about the chemical states of the particles observed. The results of this experiment are illustrated in Figure 3.7. At high temperature, metals were observed homogeneously distributed within the liquid droplets. As the sample was cooled, the liquid alloy began to decompose and Ni-rich regions formed at the edges of the particle; but the large central particle remained liquid. Further cooling caused the Ni-rich regions to grow larger. Between 755 °C and 700 °C, Cu was also observed to segregate from the core of the precipitate. Between 746 °C and 683 °C, the chemical state changed from liquid to solid, as evidenced by μ-XAS data displayed in Figure 3.7(b).

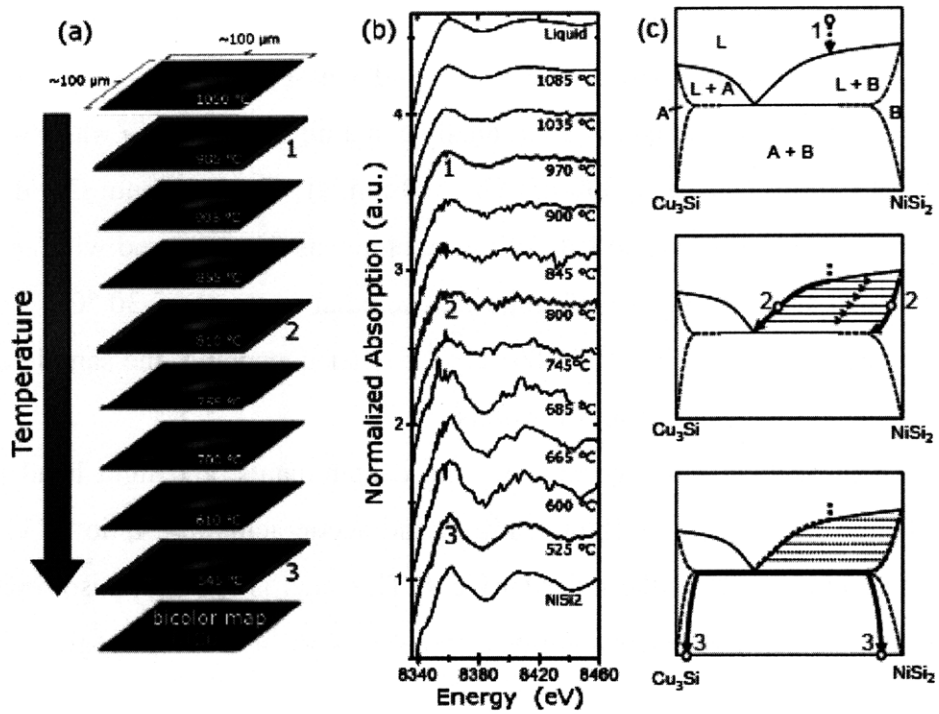

Figure 3.7: Precipitation via liquid state.

(a) Successive µ-XRF maps of a clustering of particles show its evolution from homogeneous liquid droplets (higher T) to segregated solid precipitates (lower T). The bicolor coded maps demonstrate the colocation of Ni (blue) and Cu (red) at higher T and precipitation at lower T. (b) Successive Ni K-edge µ-XANES measurements of the main particle. At top and bottom, respectively, are the liquid metal silicide and solid $NiSi_2$ standard spectra. (c) The evolution of the particle from liquid droplets to solid silicide precipitates is explained by means of a pseudo-binary phase diagram.

Figure 3.7(*c*) illustrates a schematic phase diagram of the evolution of a liquid droplet during cooling from high temperatures: decomposition of the high temperature liquid into different phases, and solidification to solid metal silicide cores. In the example shown, the composition of the particles is initially nickel-rich with respect to the eutectic composition. The particle begins as a homogeneous liquid droplet at high temperature, and is in the liquid region of the pseudo-binary phase diagram for the Cu_3Si-$NiSi_2$ system (the Si-rich corner of the Cu-Ni-Si phase diagram). Such an homogeneous phase has been predicted [105] as a precursor to the formation of the mixed-metal silicides found in as-grown solar cell material [91]. In the liquid state, the particle acts as an efficient site for the aggregation of metal atoms dissolved in the bulk by segregation gettering to the liquid droplets, driven by differential solubilities. During cooling,

relaxation gettering can also occur as the remaining dissolved species become supersaturated, and preferentially diffuse to existing defects to minimize interface strain energy [106].

The pseudo-binary phase diagram shown in Figure 3.7 corresponds to a vertical cut from the 3-dimensional ternary phase diagram from the Cu-Ni-Si system. One representation of this system is shown in Figure 3.8, which shows the liquidus contour from the ternary phase diagram for the Cu-Ni-Si system [107]. The green dashed line signifies the tie-line along which the pseudo-binary phase diagram of Figure 3.7 is taken. The pseudo-binary phase diagram for the Cu_3Si-$NiSi_2$ system is a vertical cut from the three-dimensional ternary phase diagram. Because the droplets being observed in this study are forming from dissolved species present in concentrations much less than one atomic percent, the composition of precipitates formed is confined to this vertical plane between the two silicon-rich silicides ($NiSi_2$ and Cu_3Si), prohibiting formation of the other phases observed in the more metal-rich regions of the ternary phase diagram. For this reason, the behavior of the alloy is modeled under the assumption that the composition stays in the plane of the pseudo-binary phase diagram.

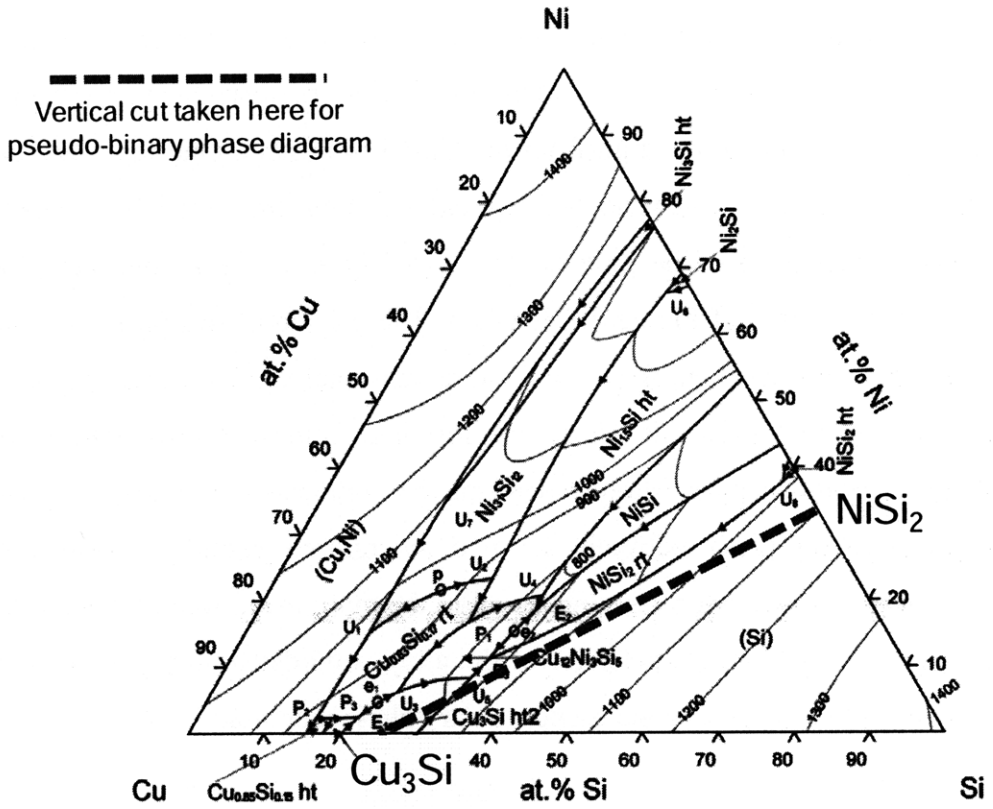

Figure 3.8: Copper Nickel Silicon ternary phase diagram.
Liquidus contour of the ternary phase diagram for the Cu-Ni-Si system, showing the location of the vertical cut that is represented in the pseudo-binary phase diagram. Reprinted from [107] with permission of ASM International®. All rights reserved.

Drawing from our experimental observations and our model using the pseudo-binary phase diagram of the Cu3Si-NiSi2 system, we can describe the formation mechanism of mixed-metal silicide particles of the type shown in Figure 3.6. Figure 3.9 shows schematically the formation of a spatially phase-segregated mixed metal silicide. First, the liquid droplet forms, either by retrograde melting, as in Figure 3.9(*b*), or by direct inclusion from the melt, as in Figure 3.9(a), and as described by Abrosimov [102]. As the liquid droplet cools and first passes through the liquidus (on either the $NiSi_2$- or Cu_3Si-rich side, depending on initial concentration of metals), a portion of the droplet solidifies, shown in Figure 3.9(*d*). Due to the high diffusivity of nickel and copper at elevated temperatures [103], significant rearrangement of the particles is possible. Experimentally, this is observed in the changing ratios of Cu and Ni in the bicolor μ-XRF maps in Figure 3.7(a). With further cooling, the initial precipitate grows, and the

composition of the remaining liquid droplet follows the liquidus towards the eutectic composition. When the eutectic point is reached on the phase diagram, further cooling causes the droplet to decompose into two solid metal silicide phases: an η-Cu_3Si phase and a mixed-metal silicide phase with a $NiSi_2$ structure, as seen in Figure 3.9(*e*).

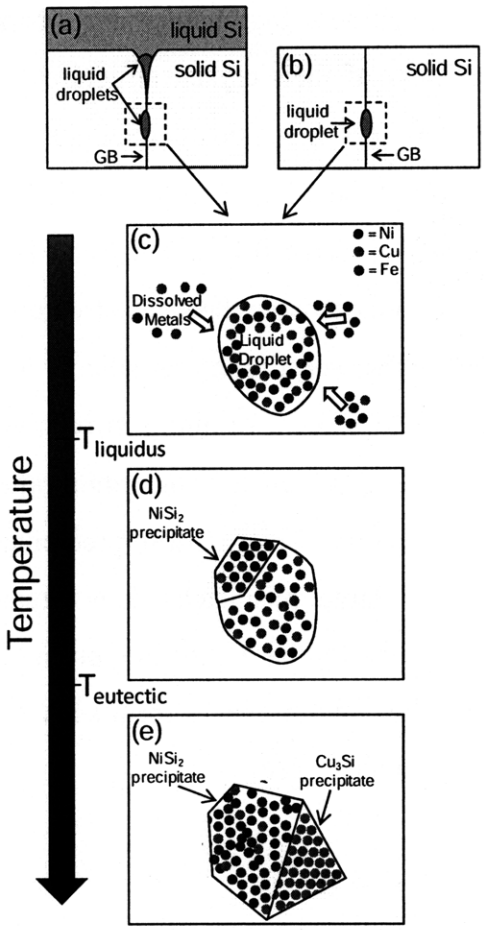

Figure 3.9: Schematic description of droplet formation, gettering, and precipitation. (a,b) Two possible formation mechanisms of liquid droplets during crystal growth: (a) direct incorporation from the melt along grain boundaries, and (b) from supersaturated metals precipitating at favorable nucleation sites along grain boundaries. (c) At high temperature, liquid droplets grow by segregation of metals from the bulk. (d) Upon cooling, as the temperature drops below the liquidus temperature (determined by the starting composition), Ni begins to precipitate into $NiSi_2$. The composition of the remaining liquid moves towards the eutectic composition. (e) At the eutectic temperature, the eutectic composition becomes unstable, and decomposes into two phases: Cu_3Si nodules surrounding a mixed-metal silicide core. The final phases are non-equilibrium phases, as the samples were not cooled sufficiently slowly to allow equilibration.

Both phases present in the precipitate ($NiSi_2$ and Cu_3Si) are known to accommodate up to atomic percents of substitutional metal species, as reported in alloy experiments [108]. The phases observed in this experiment, as well as their morphology, agree well with previous investigations of solid-phase mixed-metal silicides in silicon (see Figure 3.6, and [91],[109]).

The observed decomposition of mixed-metal silicide precipitates into two separate phases at room temperature from a single phase at high temperatures is postulated to occur in large part because of the different characters of their crystal structures. Figure 3.10 shows the crystal structures of (*a*) α-$NiSi_2$ and (*b*) η'-Cu_3Si (an intermediate temperature phase, with similar structure to the low-temperature phase of η"-Cu_3Si), along with (*c*) a mixed-metal silicide structure previously reported in [44], and (*d*) a mixed-metal silicide previously observed, but unpublished. These mixed-metal silicides have the same structure as α-$NiSi_2$, with cobalt and/or iron substituting for nickel, and copper substituting for silicon. $NiSi_2$ is a lattice-matched silicide with lattice constant close to that of silicon, resulting in relatively low interface strain energy with the bulk. On the other hand, η"-Cu_3Si has an orthorhombic crystal structure with high lattice mismatch to the silicon matrix. Thus, Cu_3Si precipitates are characterized by high interface strain. In addition, this large mismatch likely creates a large energy barrier to nucleation. Therefore, it is not surprising that Cu_3Si-like phases and $NiSi_2$-like phases prove to be incompatible at low temperatures, and prefer to form separate phases with some amount of substitutional impurities from the other species.

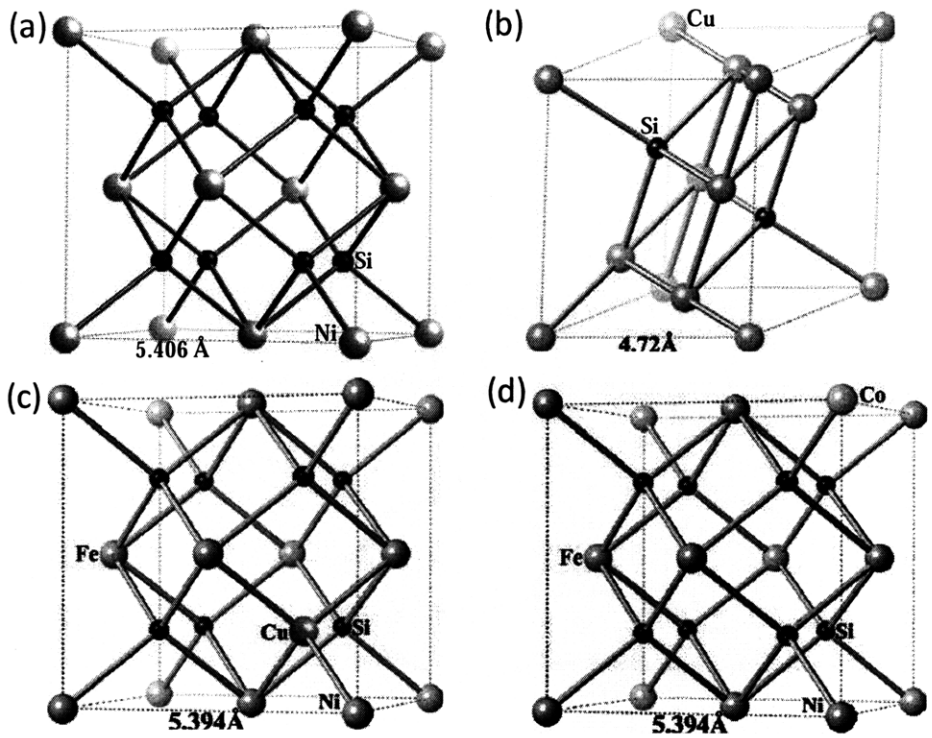

Figure 3.10: Crystal structures of precipitates observed.
(a) Ni forms a CaF_2-type $NiSi_2$ structure with lattice constant very close to that of the Si lattice. (b) Cu forms orthorhombic Cu_3Si (η'-Cu_3Si shown), which is incoherent with the Si lattice and has large interface strain. (c,d) Two examples of mixed metal silicide structures, with the $NiSi_2$ structure and substitutional Cu on the Si site (c), and Fe or Co on the Ni site (c,d). (c) reproduced from [44], with permission.

3.8 High Temperature Measurements of As-Grown mc-Si

The above results have all been obtained at the Advanced Light Source Beamline 10.3.2, using intentionally contaminated materials. Intentional contamination was required due to the larger spot size and lower photon flux at this beamline, as compared with the higher-resolution beamline 2-ID-D at the Advanced Photon Source. In this section, preliminary results are presented of high temperature, high resolution (< 1 μm) μ-XRF investigations of as-grown (i.e. non-intentionally-contaminated) mc-Si solar cell materials.

Figure 3.11 shows a grain boundary in multicrystalline silicon that was mapped (total area 50 x 60 μm^2, 0.5 x 0.5 μm^2) steps while cooling from high temperature. Three detector channels are shown: Fe-Kα, Cu-Kα, and elastically scattered beam signal. The Elastic channel can be used to give information about the location of the grain boundary. As the temperature

decreases, the sample is mapped from bottom to top. Thus the lowest regions of the map are highest temperature, and there is a time- and temperature-gradient moving up the map. The red lines in the map denote the approximate temperatures of several vertical positions.

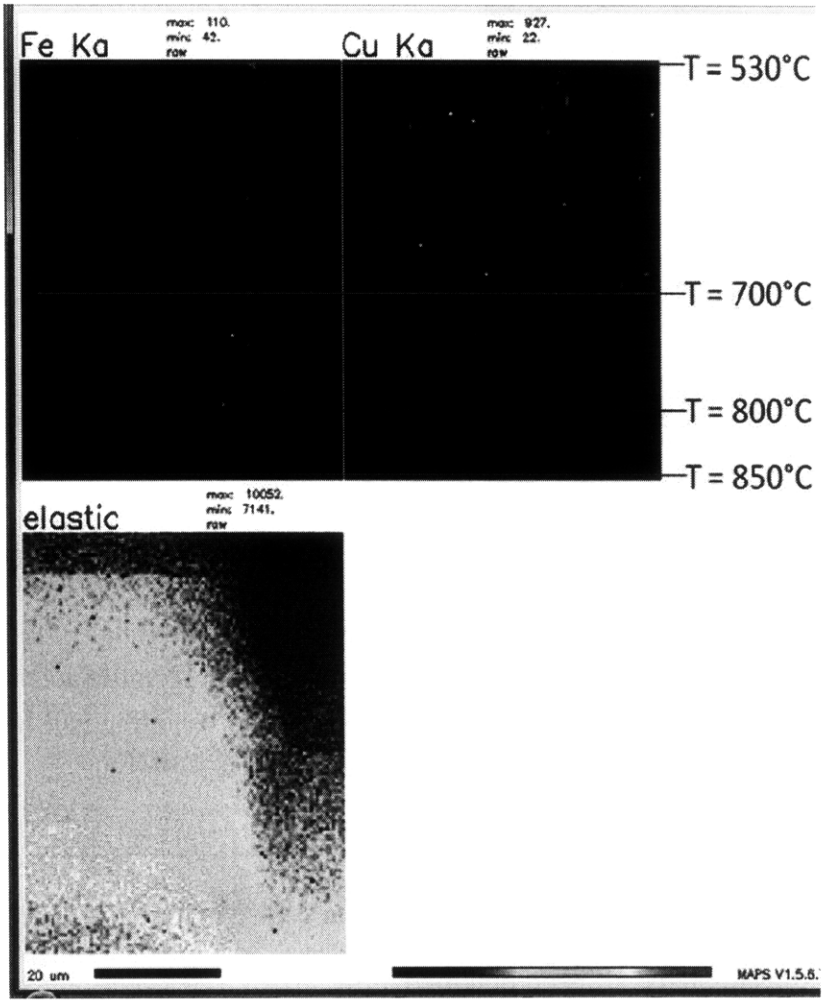

Figure 3.11: Precipitate formation upon cooling in as-grown mc-Si sample.
The sample was cooled during mapping, and mapping occurred from the bottom line upwards. Above 800°C, both Cu and Fe are dissolved in the Si. Below 800°C, Fe begins to precipitate along the grain boundary. Below 700°C, Cu also precipitates out of solution along the GB and in the bulk. The red lines denote the temperatures at various locations on the map.

At the high starting temperature of 850°C (bottom of the map), both Fe and Cu are dissolved within the silicon matrix. As temperature decreases, two clear transition temperatures are evident. First, at ~800°C, Fe begins to precipitate along the vertical GB (seen in the elastic map below). Between 800°C and 700°C, copper is still dissolved, while Fe forms precipitates along the grain boundary. Finally, below 700°C, Cu also precipitates out of the solid solution,

forming particles both along the grain boundary, as well as within the grain. The observation of Fe precipitating before Cu can be explained due to its lower solubility in Si. Thus, it reaches a supersaturated state at a higher temperature than Cu, providing a driving force for precipitation.

These results are the first high temperature measurements obtained at Beamline 2-ID-D. High temperature measurements on this beamline proved harder than expected, due to the exaggerated effect of thermal drift: at smaller length scales (both smaller particles, on the order of 10-100 nm, and smaller spot size, on the order of 250 nm), thermal expansion on the order of 5 μm can move the scan area completely off of a particle of interest. Thus, tracking the evolution of small particles with the current setup was abandoned for the approach of taking large maps, as seen in Figure 3.11.

This could potentially be addressed by the creation of a new sample mounting system with lower coefficient of thermal expansion (e.g. Ti instead of Al), as was implemented for Beamline 10.3.2. Additionally, a complete re-design of the sample stage to eliminate unnecessary features and reduce its overall size could help reduce the detrimental effects of thermal drift.

CHAPTER

4

CONCLUSIONS AND FUTURE WORK

4.1 Conclusions

4.1.1 Development of X-ray Microprobe High Temperature Sample Stage

The development of the *in situ* high temperature sample stage for two X-ray microprobe beamlines has allowed for novel studies in crystalline silicon at temperatures ranges (500 – 1200°C) representative of actual manufacturing processes.

The stage has been shown to achieve high temperatures in a controlled ambient, with sufficient stability to track the evolution of micron-scale features over these temperatures. The ability has also been demonstrated to map *in situ* the distribution of 3d transition metal elements, at high temperature and over large volumes of material. High temperature μ-XAS was used to obtain the first measurements of a liquid metal-silicon phase. Further application of this technique to crystalline silicon may lead to a thorough understanding of efficiency limiting defects and provide new pathways to improve device performance. This high temperature technique combined with X-ray beamline capabilities opens the possibility to study important phenomena occurring at high temperatures in a wide range of materials.

4.1.2 High Temperature Investigations of Crystalline Silicon

With a deeper understanding of formation and behavior of liquid droplets in crystalline silicon, new insight can be offered into several unresolved questions concerning the nature and performance of mc-Si. First, the complex morphology of multiple-metal silicide precipitates frequently observed [45,110-115] in these materials can be explained. The precipitates analyzed with high spatial resolution techniques [90,110,111] exhibit the same nanoscale compositional

variation evident in the low-temperature μ-XRF maps in Figure 3.7. With intentional engineering employing these new phenomena, one may better control the distribution of deleterious impurities such as iron, e.g., by coaxing them into isolated precipitates via solid-liquid segregation (shown in Figure 3.5 and Figure 3.9). Alternatively, one may diminish the concentration of deleterious impurities incorporated into the material by reducing the density of liquid droplet precipitation sites (high-energy grain boundaries) or reducing the density of liquid droplets themselves, e.g., reducing the concentrations of species that exhibit retrograde melting and high bulk solubilities.

This effect should have wide applicability beyond the 3d transition metals in silicon; by comparing the impurity solubility data [94] and phase diagrams [101] as shown in Figure 3.4, it is apparent that a very similar behavior should occur in other materials wherein the enthalpy of point defect formation is large, including germanium doped with large concentrations of copper, silver, lithium, antimony, nickel, zinc, and lead [94]. By precipitating impurities as liquid droplets within a solid matrix, there exist unique opportunities to tailor the location and nanoscale phase morphology of embedded particles within semiconductors. The formation of dual-compound nanoparticles, as shown in Figure 3.7, is possible by controlling the absolute and relative concentrations of dissolved impurities as well as the cooling rate. Additionally, non-equilibrium phases can also be formed in these particles, by implementing a relatively quick cool between the phase transition and room temperatures.

In conclusion, the observation and elucidation of retrograde melting in a semiconductor material provides valuable new insight into the area of semiconductor processing. The presence of liquid droplets inside the solid semiconductor presents opportunities for controlling detrimental impurity species. The subsequent micro/nanoscale phase decomposition of liquid in semiconductors offers a promising new direction for tailoring the properties of materials at the sub-micrometer scale.

4.2 Future Work

The work presented in this thesis provides a new characterization tool for studying crystalline silicon (and potentially other materials systems). Additionally, novel results concerning the thermodynamics and kinetics of metal impurities in silicon have been produced. I envision the continuation of this work in several areas being of potential benefit.

4.2.1 Further High Temperature Technique Development

While we have demonstrated that the *in situ* X-ray microprobe sample heating stage enables studies of crystalline silicon under realistic operating conditions, there is much room for improvement.

The first area of such improvement could be refining and optimizing the current setup. For example, one current limitation to spatial resolution at high temperature comes from the thermal-expansion-induced vibrations of the on/off control duty cycle of the heating element. Changing the control loop to enable variable current through the heating element (as opposed to simply varying the on/off duty cycle) could play a large part in eliminating these vibrations.

Second, continued work on optimizing the window material to reduce its thickness and increase overall signal-to-noise ratio of measurements could allow detection of smaller quantities of impurities (e.g. in as-grown materials) and allow for quicker measurements.

Further reduction of thermal drift due to thermal expansion could be envisioned by a complete redesign of the in situ sample stage. A new design could incorporate a much lower coefficient of thermal expansion (CTE) material (an example of such a material is Invar, with a coefficient of thermal expansion that can approach $1x10^{-6}$ K^{-1}).

A final experimental setup that could be envisioned would be the implementation of an *in situ* crystal growth sample stage for use at the synchrotron beamline. There are countless technical difficulties involved with creating a sample stage to heat a sample about 1400°C and contain liquid Si, while maintaining a transparent window for incoming and outgoing X-rays. However, the insight that could be provided into crystal growth mechanisms would be invaluable. Such a setup could verify the model of Abrosimov concerning impurity segregation at grain boundaries during crystal growth [102]. It could also provide further insight into the behavior of metal impurities during directional solidification, leading to a detailed understanding of why segregation coefficients are often lower than expected [116]. In theory, this melting-stage could also be used to study the carbothermic reduction process used in the creation of metallurgical grade silicon from silicon-bearing rocks and minerals, leading to a better understanding of the behavior of impurities during the earliest silicon feedstock refining steps.

4.2.2 Interactions of metals

In addition to further development of the high temperature sample stage, further work could also include designed experiments that further elucidate the interactions of various transition metals during solar cell processing. Of particular interest could be the effect of large amounts of copper and nickel present in feedstock materials on the total incorporation of iron. While Cu and Ni are high solubility, fast-diffusing metals that are easily gettered during later solar cell processing, it is possible that their presence is leading to increased incorporation of iron (a lower solubility, slowly-diffusing metal), which is typically much more detrimental to solar cell performance. Crystal growth experiments could be envisioned in which varying combinations and amounts of Cu, Ni, and Fe are present in the melt, and the incorporation of Fe is studied (both by bulk methods such as mass spectroscopy, and by microprobe measurements to determine spatial distributions).

REFERENCES

[1] EIA - Short-Term Energy Outlook - Real Petroleum Prices. Accessed 3 Apr 2009 <http://www.eia.doe.gov/emeu/steo/pub/fsheets/real_prices.html>.

[2] E&E: U.S. Energy Flow — 2002. Accessed 3 Apr 2009 <https://eed.llnl.gov/flow/02flow.php>.

[3] Energy Information Administration - International Total Primary Energy Consumption and Energy Intensity Data. Accessed 9 Apr 2009 <http://www.eia.doe.gov/emeu/international/energyconsumption.html>.

[4] S. Deng. *Stochastic models of energy commodity prices and their applications: Mean-reversion with jumps and spikes*, University of California Energy Institute (2000).

[5] E. Regnier. *Energy Economics* **29**, 405-427 (2007).

[6] R. Alley, T. Berntsen, N.L. Bindoff, Z. Chen, A. Chidthaisong, and P. Friedlingstein. *Climate Change* 2-18 (2007).

[7] W.A. Hermann. *Energy* **31**, 1349-1366 (2006).

[8] J.E. Katz, T.R. Gingrich, E.A. Santori, and N.S. Lewis. *Energy & Environmental Science* **2**, 103-112 (2009).

[9] File:PnJunction-PV-E.PNG - Wikimedia Commons. Accessed 3 Apr 2009 <http://commons.wikimedia.org/wiki/File:PnJunction-PV-E.PNG>.

[10] M.A. Green. *Silicon solar cells: advanced principles & practice*, Centre for Photovoltaic Devices and Systems Sydney (1995).

[11] C.P. Khattak, D.B. Joyce, and F. Schmid. *Solar Energy Materials and Solar Cells* **74**, 77-89 (2002).

[12] P. Woditsch and W. Koch. *Solar Energy Materials and Solar Cells* **72**, 11-26 (2002).

[13] S.O. Kasap and P. Capper. *Springer handbook of electronic and photonic materials*, (2006).

[14] E. Yablonovitch and G. Cody. *Electron Devices, IEEE Transactions on* **29**, 300-305 (1982).

[15] K. Graff. *Metal impurities in silicon-device fabrication*, New York: Springer, Berlin (2000).

[16] D. Macdonald, A. Cuevas, and F. Ferrazza. *Solid-State Electronics* **43**, 575-581 (1999).

[17] M.J. Kerr, J. Schmidt, A. Cuevas, and J.H. Bultman. *Journal of Applied Physics* **89**, 3821-3826 (2001).

[18] J. Chen, D. Yang, Z. Xi, and T. Sekiguchi. *Physica B: Condensed Matter* **364**, 162-169 (2005).

[19] O.F. Vyvenko, T. Buonassisi, A.A. Istratov, E.R. Weber, M. Kittler, and W. Seifert. *Journal of Physics-Condensed Matter* **14**, 13079-13086 (2002).

[20] K. McLean, C. Morrow, and D. Macdonald. "Activation Energy for the Hydrogenation of Iron in P-Type Crystalline Silicon Wafers." *Conference Record of the 2006 IEEE 4th World Conference on Photovoltaic Energy Conversion* 1122-1125 (2006).

[21] T. Buonassisi, A.A. Istratov, S. Peters, C. Ballif, J. Isenberg, S. Riepe, W. Warta, R. Schindler, G. Willeke, Z. Cai, B. Lai, and E.R. Weber. *Applied Physics Letters* **87**, 121918 (2005).

[22] C. Wadia, A.P. Alivisatos, and D.M. Kammen. *Environmental Science and Technology* **43**, 2072-2077 (2009).
[23] C.J. Brabec. *Solar Energy Materials and Solar Cells* **83**, 273-292 (2004).
[24] M. Grätzel. *Journal of Photochemistry and Photobiology A: Chemistry* **164**, 3-14 (2004).
[25] B. Tian, X. Zheng, T.J. Kempa, Y. Fang, N. Yu, G. Yu, J. Huang, and C.M. Lieber. *Nature* **449**, 885-889 (2007).
[26] A.J. Nozik. *Physica E: Low-dimensional Systems and Nanostructures* **14**, 115-120 (2002).
[27] Trends in Photovoltaics Applications. Accessed 3 Apr 2009 <http://www.iea-pvps.org/products/download/rep1_17.pdf>.
[28] G. Willeke. "The Fraunhofer ISE roadmap for crystalline silicon solar cell technology." *Proceedings of the Twenty-Ninth IEEE Photovoltaic Specialists Conference* 53-57 (2002).
[29] M.A. Green. *Solar cells*, Prentice-Hall Kensington (1982).
[30] D. Clugston and P. Basore. "PC1D version 5: 32-bit solar cell modeling on personal computers." *Proceedings of the Twenty-Sixth IEEE Photovoltaic Specialists Conference* 207-210 (1997).
[31] V. Kveder, M. Kittler, and W. Schröter. *Physical Review B* **63**, 115208 (2001).
[32] G. Stokkan, S. Riepe, O. Lohne, and W. Warta. *Journal of Applied Physics* **101**, 053515-9 (2007).
[33] S.A. McHugo, H. Hieslmair, and E.R. Weber. *Applied Physics A: Materials Science & Processing* **64**, 127-137 (1997).
[34] G.W.C. Kaye. *Kaye & Laby Tables of Physical & Chemical Constants*, National Physical Laboratory (1995).
[35] A.A. Istratov, T. Buonassisi, R.J. McDonald, A.R. Smith, R. Schindler, J.A. Rand, J.P. Kalejs, and E.R. Weber. *Journal of Applied Physics* **94**, 6552-6559 (2003).
[36] P.S. Plekhanov, R. Gafiteanu, U.M. Gosele, and T.Y. Tan. *Journal of Applied Physics* **86**, 2453-2458 (1999).
[37] W.B. Henley and D.A. Ramappa. *Journal of Applied Physics* **82**, 589-594 (1997).
[38] M.D. Pickett and T. Buonassisi. *Applied Physics Letters* **92**, 122103 (2008).
[39] D. Macdonald and L.J. Geerligs. *Applied Physics Letters* **85**, 4061-4063 (2004).
[40] A. Istratov, H. Hieslmair, and E. Weber. *Applied Physics A-Materials Science & Processing* **70**, 489-534 (2000).
[41] A.A. Istratov and E.R. Weber. *Applied Physics A-Materials Science & Processing* **66**, 123-136 (1998).
[42] T. Buonassisi, A.A. Istratov, M.D. Pickett, M. Heuer, J.P. Kalejs, G. Hahn, M.A. Marcus, B. Lai, Z. Cai, S.M. Heald, T.F. Ciszek, R.F. Clark, D.W. Cunningham, A.M. Gabor, R. Jonczyk, S. Narayanan, E. Sauar, and E.R. Weber. *Progress in Photovoltaics: Research and Applications* **14**, 513-531 (2006).
[43] T. Buonassisi, A.A. Istratov, M.A. Marcus, B. Lai, Z.H. Cai, S.M. Heald, and E.R. Weber. *Nature Materials* **4**, 676-679 (2005).
[44] T. Buonassisi, M. Heuer, A.A. Istratov, M.D. Pickett, M.A. Marcus, B. Lai, Z. Cai, S.M. Heald, and E.R. Weber. *Acta Materialia* **55**, 6119-6126 (2007).
[45] M. Heuer, T. Buonassisi, A.A. Istratov, M.D. Pickett, M.A. Marcus, A.M. Minor, and E.R. Weber. *Journal of Applied Physics* **101**, 123510 (2007).
[46] T. Buonassisi, A.A. Istratov, M.D. Pickett, M.A. Marcus, T.F. Ciszek, and E.R. Weber. *Applied Physics Letters* **89**, 042102 (2006).

[47] H.J. Möller, L. Long, M. Werner, and D. Yang. *physica status solidi (a)* **171**, 175-189 (1999).
[48] H.J. Möller, C. Funke, A. Lawerenz, S. Riedel, and M. Werner. *Solar Energy Materials and Solar Cells* **72**, 403-416 (2002).
[49] A.K. Søiland, E.J. Øvrelid, T.A. Engh, O. Lohne, J.K. Tuset, and Ø. Gjerstad. *Materials Science in Semiconductor Processing* **7**, 39-43 (2004).
[50] J. Rakotoniaina, O. Breitenstein, M. Werner, M. Hejjo Al-Rifai, T. Buonassisi, M. Pickett, M. Ghosh, and A. Müller. "Distribution and formation of silicon carbide and silicon nitride precipitates in block-cast multicrystalline silicon." *Proceedings of the 20th European Photovoltaic Solar Energy Conference* (2005).
[51] N. Yuge, M. Abe, K. Hanazawa, H. Baba, N. Nakamura, Y. Kato, Y. Sakaguchi, S. Hiwasa, and F. Aratani. *Progress in Photovoltaics: Research and Applications* **9**, 203-209 (2001).
[52] S.C. Singhal. *Solid State Ionics* **135**, 305-313 (2000).
[53] O. Yamamoto. *Electrochimica Acta* **45**, 2423-2435 (2000).
[54] M. Peña, J. Gómez, and J. Fierro. *Applied Catalysis A: General* **144**, 7-57 (1996).
[55] P.D.F. Vernon, M.L.H. green, A.K. Cheetham, and A.T. Ashcroft. *Catalysis Letters* **6**, 181-186 (1990).
[56] S.R. Wenham and M.A. Green. *Progress in Photovoltaics: Research and Applications* **4**, 3-33 (1996).
[57] S.A. McHugo, A.C. Thompson, A. Mohammed, G. Lamble, I. Perichaud, S. Martinuzzi, M. Werner, M. Rinio, W. Koch, H. Hoefs, and C. Haessler. *Journal of Applied Physics* **89**, 4282-4288 (2001).
[58] A. Manceau, M.A. Marcus, and N. Tamura. *Reviews in Mineralogy and Geochemistry* **49**, 341-428 (2002).
[59] W. Yun, B. Lai, Z. Cai, J. Maser, D. Legnini, E. Gluskin, Z. Chen, A.A. Krasnoperova, Y. Vladimirsky, F. Cerrina, E. Di Fabrizio, and M. Gentili. *Review of Scientific Instruments* **70**, 2238-2241 (1999).
[60] K.M. Kemner, S.D. Kelly, B. Lai, J. Maser, E.J. O'Loughlin, D. Sholto-Douglas, Z. Cai, M.A. Schneegurt, C.F. Kulpa, and K.H. Nealson. *Science* **306**, 686-687 (2004).
[61] M. Naghedolfeizi, J.S. Chung, R. Morris, G.E. Ice, W.B. Yun, Z. Cai, and B. Lai. *Journal of Nuclear Materials* **312**, 146-155 (2003).
[62] T. Buonassisi, A.A. Istratov, M. Heuer, M.A. Marcus, R. Jonczyk, J. Isenberg, B. Lai, Z.H. Cai, S. Heald, W. Warta, R. Schindler, G. Willeke, and E.R. Weber. *Journal of Applied Physics* **97**, 074901 (2005).
[63] T. Buonassisi, M.A. Marcus, A.A. Istratov, M. Heuer, T.F. Ciszek, B. Lai, Z.H. Cai, and E.R. Weber. *Journal of Applied Physics* **97**, 063503 (2005).
[64] J.A. Mavrogenes, A.J. Berry, M. Newville, and S.R. Sutton. *American Mineralogist* **87**, 1360-1364 (2002).
[65] A.J. Berry, A.C. Hack, J.A. Mavrogenes, M. Newville, and S.R. Sutton. *American Mineralogist* **91**, 1773-1782 (2006).
[66] S.R. Sutton, P.M. Bertsch, M. Newville, M. Rivers, A. Lanzirotti, and P. Eng. *Reviews in Mineralogy and Geochemistry* **49**, 429-483 (2002).
[67] A.J. Berry, J.M.G. Shelley, G.J. Foran, H.S.C. O'Neill, and D.R. Scott. *Journal of Synchrotron Radiation* **10**, 332-336 (2003).
[68] F. Farges, A. Flank, P. Lagarde, and F. Ténégal. *Journal of Synchrotron Radiation* **6**, 193-194 (1999).

[69] G. Jacobs and I. Egry. *Physical Review B* **59**, 3961-3968 (1999).
[70] S.G. Eeckhout, B. Gorges, L. Barthe, O. Pelosi, O. Safonova, and G. Giuli. *Journal of Synchrotron Radiation* **15**, 489-494 (2008).
[71] M. Kunz, A.A. MacDowell, W.A. Caldwell, D. Cambie, R.S. Celestre, E.E. Domning, R.M. Duarte, A.E. Gleason, J. M. Glossinger, N. Kelez, D. W. Plate, T. Yu, J. M. Zaug, H. A. Padmore, R. Jeanloz, A. P. Alivisatos, and S.M. Clark. *J. Synchrotron Rad.* **12**, 650-658 (2005).
[72] E. de Smit, I. Swart, J.F. Creemer, G.H. Hoveling, M.K. Gilles, T. Tyliszczak, P.J. Kooyman, H.W. Zandbergen, C. Morin, B.M. Weckhuysen, and F.M.F. de Groot. *Nature* **456**, 222-225 (2008).
[73] R.T.K. Baker and P.S. Harris. *Journal of Physics E: Scientific Instruments* **5**, 793-797 (1972).
[74] C. Hayzelden, J.L. Batstone, and R.C. Cammarata. *Applied Physics Letters* **60**, 225-227 (1992).
[75] J.F. Creemer, S. Helveg, G. Hoveling, S. Ullmann, A. Molenbroek, P. Sarro, and H. Zandbergen. *Ultramicroscopy* **108**, 993-998 (2008).
[76] M.A. Marcus, A.A. MacDowell, R. Celestre, A. Manceau, T. Miller, H.A. Padmore, and R.E. Sublett. *Journal of Synchrotron Radiation* **11**, 239-247 (2004).
[77] W. Yun, B. Lai, D. Shu, A. Khounsary, Z. Cai, J. Barraza, and D. Legnini. *Review of Scientific Instruments* **67**, 3373-3376 (1996).
[78] R. Hull, ed. *Properties of Crystalline Silicon*, London: The Institution of Electrical Engineers (1999).
[79] F.A. Cunnold. *Proceedings of the Royal Society of London. Series A, Mathematical and Physical Sciences* **152**, 64-80 (1935).
[80] H.J. Kostkowski and R.D. Lee. *NBS Monograph 41, National Bureau of Standards, Washington, DC*, (1962).
[81] T. Satō. *Japanese Journal of Applied Physics* **6**, 339-347 (1967).
[82] M.G. Cooper, B.B. Mikic, and M.M. Yovanovich. *International Journal of Heat and Mass Transfer* **12**, 279-300 (1969).
[83] http://cxro.lbl.gov/. Center for X-Ray Optics | Pioneering Soft X-Ray Optics Research and Applications. Accessed 9 Mar 2009 <http://www.cxro.lbl.gov/>.
[84] G.E. Rhead. *Surface Science* **47**, 207-221 (1975).
[85] N. Gjostein. "Short circuit diffusion." *Diffusion* 241-274 Metals Park, Ohio: American Society for Metals (ASM) (1973).
[86] B. Ravel and M. Newville. *Journal of Synchrotron Radiation* **12**, 537-541 (2005).
[87] N. Avraham, B. Khaykovich, Y. Myasoedov, M. Rappaport, H. Shtrikman, D.E. Feldman, T. Tamegai, P.H. Kes, M. Li, M. Konczykowski, K. van der Beek, and E. Zeldov. *Nature* **411**, 451-454 (2001).
[88] A.L. Greer. *Nature* **404**, 134-135 (2000).
[89] D.H. Speidel and R.H. Nafziger. *Science* **152**, 1367-1368 (1966).
[90] K. Ryoo, R. Drosd, and W. Wood. *Journal of Applied Physics* **63**, 4440-4443 (1988).
[91] T. Buonassisi, M. Heuer, A.A. Istratov, M.D. Pickett, M.A. Marcus, B. Lai, Z. Cai, S.M. Heald, and E.R. Weber. *Acta Materialia* **55**, 6119-6126 (2007).
[92] D. Gilles, E.R. Weber, and S. Hahn. *Physical Review Letters* **64**, 196 (1990).
[93] S.M. Myers, M. Seibt, and W. Schroter. *Journal of Applied Physics* **88**, 3795-3819 (2000).
[94] F.A. Trumbore. *The Bell System Technical Journal* **39**, 205-233 (1960).

[95] D. Macdonald, A. Cuevas, A. Kinomura, Y. Nakano, and L.J. Geerligs. *Journal of Applied Physics* **97**, 033523 (2005).
[96] T.F. Ciszek. *Solar Cells* **21**, 81-98 (1987).
[97] F. Stein, G. Sauthoff, and M. Palm. *Journal of Phase Equilibria* **23**, 480-494 (2002).
[98] S. Wagner and D.A. Rigney. *Metallurgical Transactions* **5**, 2155-2160 (1974).
[99] R. Ferro, A. Saccone, S. Delfino, A.M. Cardinale, and D. Maccio. *Metallurgical and Materials Transactions B-Process Metallurgy and Materials Processing Science* **27**, 979-986 (1996).
[100] M. Stier and M. Rettenmayr. *Journal of Crystal Growth* **311**, 137-140 (2008).
[101] H. Okamoto. *Desk Handbook: Phase Diagrams for Binary Alloys*, ASM International (2000).
[102] N.V. Abrosimov, A.V. Bazhenov, and V.A. Tatarchenko. *Journal of Crystal Growth* **82**, 203-208 (1987).
[103] E.R. Weber. *Applied Physics A-Materials Science & Processing* **30**, 1-22 (1983).
[104] E. Nes and J. Washburn. *Journal of Applied Physics* **44**, 3682-3688 (1973).
[105] M. Heuer, S. Langkau, T. Buonassisi, A.A. Istratov, A. Minor, and E. Weber. *Proceedings, 22nd European Photovoltaics Solar Energy Conference* (2007).
[106] A.A. Istratov, W. Huber, and E.R. Weber. *Applied Physics Letters* **85**, 4472-4474 (2004).
[107] Y.A. Chang, J.P. Neumann, A. Mikula, and D. Goldberg. *Phase Diagrams and Thermodynamic Properties of Ternary Copper-Metal Systems, INCRA Monograph VI* (1979).
[108] S. Langkau, M. Heuer, H. Höbler, K. Bente, and G. Kloess. *Journal of Alloys and Compounds* **474**, 334-340 (2008).
[109] M. Heuer, T. Buonassisi, A.A. Istratov, M.D. Pickett, M.A. Marcus, A.M. Minor, and E.R. Weber. *Journal of Applied Physics* **101**, 123510 (2007).
[110] T. Buonassisi, A.A. Istratov, M.D. Pickett, M. Heuer, J.P. Kalejs, G. Hahn, M.A. Marcus, B. Lai, Z. Cai, S.M. Heald, T.F. Ciszek, R.F. Clark, D.W. Cunningham, A.M. Gabor, R. Jonczyk, S. Narayanan, E. Sauar, and E.R. Weber. *Progress in Photovoltaics* **14**, 513-531 (2006).
[111] M. Heuer, T. Buonassisi, M.A. Marcus, A.A. Istratov, M.D. Pickett, T. Shibata, and E.R. Weber. *Physical Review B* **73**, 235204 (2006).
[112] A.G. Cullis and L.E. Katz. *Philosophical Magazine* **30**, 1419-1443 (1974).
[113] C. Colliex, J.L. Maurice, and D. Ugarte. *Ultramicroscopy* **29**, 31-43 (1989).
[114] D.R. Khanal, T. Buonassisi, M.A. Marcus, A.A. Istratov, and E.R. Weber. *Applied Physics Letters* **90**, 102110 (2007).
[115] H. Nordmark, M. Di Sabatino, E. Øvrelid, J.C. Walmsley, and R. Holmestad. *Proceedings, 22nd European Photovoltaics Solar Energy Conference* 1710 (2007).
[116] D. Macdonald, A. Cuevas, A. Kinomura, Y. Nakano, and L.J. Geerligs. *Journal of Applied Physics* **97**, 033523 (2005).